

# Chemical probes of turbulence in the diffuse medium: the TDR model

B. Godard<sup>1</sup>, E. Falgarone<sup>1</sup>, and G. Pineau des Forêts<sup>2,1</sup>

<sup>1</sup> LERMA, CNRS UMR 8112, École Normale Supérieure & Observatoire de Paris, Paris, France

<sup>2</sup> Institut d'Astrophysique Spatiale, CNRS UMR 8617, Université Paris-Sud, Orsay, France

Received 28 January 2014 / Accepted 19 July 2014

## Abstract

**Context.** Tens of light hydrides and small molecules have now been detected over several hundreds sightlines sampling the diffuse interstellar medium (ISM) in both the Solar neighbourhood and the inner Galactic disk.

**Aims.** These new data confirm the limitations of the traditional chemical pathways driven by the UV photons and the cosmic rays (CR) and the need for additional energy sources, such as turbulent dissipation, to open highly endoenergetic formation routes. The goal of the present paper is to further investigate the link between specific species and the properties of the turbulent cascade in particular its space-time intermittency.

**Methods.** We have analysed ten different atomic and molecular species in the framework of the updated model of turbulent dissipation regions (TDR). We study the influence on the abundances of these species of parameters specific to chemistry (density, UV field, and CR ionisation rate) and those linked to turbulence (the average turbulent dissipation rate, the dissipation timescale, and the ion-neutral velocity drift in the regions of dissipation).

**Results.** The most sensitive tracers of turbulent dissipation are the abundances of  $\text{CH}^+$  and  $\text{SH}^+$ , and the column densities of the  $J = 3, 4, 5$  rotational levels of  $\text{H}_2$ . The abundances of CO,  $\text{HCO}^+$ , and the intensity of the  $158\ \mu\text{m}$  [CII] emission line are significantly enhanced by turbulent dissipation. The vast diversity of chemical pathways allows the independent determinations of free parameters never estimated before: an upper limit to the average turbulent dissipation rate,  $\bar{\epsilon} \lesssim 10^{-23}\ \text{erg cm}^{-3}\text{s}^{-1}$  for  $n_{\text{H}}=20\ \text{cm}^{-3}$ , from the  $\text{CH}^+$  abundance; an upper limit to the ion-neutral velocity drift,  $v_{\text{in}} \lesssim 3.5\ \text{km s}^{-1}$ , from the  $\text{SH}^+$  to  $\text{CH}^+$  abundance ratio; and a range of dissipation timescales,  $100 \lesssim \tau_v \lesssim 1000\ \text{yr}$ , from the CO to  $\text{HCO}^+$  abundance ratio. For the first time, we reproduce the large abundances of CO observed on diffuse lines of sight, and we show that CO may be abundant even in regions with UV-shieldings as low as  $5 \times 10^{-3}\ \text{mag}$ . The best range of parameters also reproduces the abundance ratios of OH,  $\text{C}_2\text{H}$ , and  $\text{H}_2\text{O}$  to  $\text{HCO}^+$  and are consistent with the known properties of the turbulent cascade in the Galactic diffuse ISM.

**Conclusions.** Our results disclose an unexpected link between the dissipation of turbulence and the emergence of molecular richness in the diffuse ISM. Some species, such as  $\text{CH}^+$  or  $\text{SH}^+$ , turn out to be unique tracers of the energy trail in the ISM. In spite of some degeneracy, the properties of the turbulent cascade, down to dissipation, can be captured through specific molecular abundances.

**Key words.** Astrochemistry - Turbulence - ISM: molecules - ISM: kinematics and dynamics - ISM: structure - ISM: clouds

## 1. Introduction

Turbulence in galaxies stands at the crossroad of a wide variety of cosmic processes: star and planet formation, galactic dynamos, magnetic reconnection, to name a few. It has a strong interplay, not only with gravity and magnetic fields, but also with the microphysics of gas because the scales at which it dissipates are close to the mean free path of atoms and molecules. The turbulent cascade in galaxies therefore channels huge amounts of supra-thermal kinetic energy from the large scales at which it is fed to those at which atoms and molecules interact.

This property of the turbulent cascade has started to be exploited to elucidate the long-standing puzzle raised by the large abundances of many molecular species that have been detected in the diffuse medium:  $\text{CH}^+$  (Crane et al. 1995; Gredel 1997; Weselak et al. 2008; Falgarone et al. 2010a; Godard et al. 2012),  $\text{HCO}^+$  (Lucas & Liszt 1996; Godard et al. 2010), CO (Sheffer et al. 2008; Liszt et al. 2010), SH and  $\text{H}_2\text{S}$  (Neufeld et al. 2012),  $\text{SH}^+$  (Godard et al. 2012), CN, HCN, and HNC (Liszt & Lucas 2001; Godard et al. 2010). Indeed these abundances cannot be understood in the framework of UV-driven chemistry because their formation proceeds through highly endoenergetic reactions that cannot be activated at the

low temperature of the diffuse interstellar medium (ISM). These findings are not specific to the Milky Way. Large abundances of  $\text{CH}^+$  are now observed in the diffuse medium of external galaxies where the  $\text{CH}^+(1-0)$  line is observed in absorption against the bright dust continuum emission of nearby starbursts: Arp 220 (Rangwala et al. 2011); Mrk231 (van der Werf et al. 2010); and M82, Circinus, and NGC4945 (Falgarone et al., in prep.).

It has been proposed that the bursts of turbulent dissipation (i.e. its property of space-time intermittency) sufficiently heat the diffuse gas locally to produce the observed abundances (Joulain et al. 1998). This would explain why the diffuse ISM is, occasionally, such a strong emitter in the pure rotational lines of  $\text{H}_2$  (Falgarone et al. 2005; Ingalls et al. 2011). Godard et al. (2009, hereafter Paper I) have improved the model proposed by Joulain et al. (1998) and set up global models of random sight lines across the medium that sample (i) the active dissipative regions driving a non-equilibrium warm chemistry, (ii) the regions in chemical and thermal relaxation that develop after the extinction of the dissipation bursts, and (iii) the ambient phase characterised by UV-driven chemistry. Although still idealised in some respects, these models take the energetic constraints provided by the turbulent cascade into account. Interestingly, it is found that

less than a few percent of the turbulent energy, on average, is sufficient to drive the warm chemistry at the observed level, the rest being radiated away mostly in the pure rotational lines of  $\text{H}_2$  and [CII] fine-structure line emission. Moreover, the comparison of the model predictions to observations clearly favours a turbulent dissipation dominated by ion-neutral friction in structures as small as  $\sim 100$  au.

In this paper, we further explore the models of Paper I and take advantage of the impressive amount of new data obtained on light molecular hydrides in the diffuse medium with *Herschel*. We compare the predictions of the TDR model to these observations, and to older data sets on CO and  $\text{HCO}^+$ . An overview of the information directly inferred from the absorption spectroscopy data is given in Sect. 2. The main characteristics of the model are summarised in Sect. 3. In Sects. 4 to 8, we explore the parameter space over large domains and use the model predictions to identify molecular species (and pairs of species) that can be used as specific diagnostics of the turbulence in the diffuse ISM. Finally, in Sect. 9, we discuss the overall coherence of the parameters of the turbulence inferred from the light hydride and CO molecular abundances. The recent refinements of the dynamical and chemical prescriptions of the TDR model are given in the Appendices.

## 2. Observational constraints on the parameter space to explore

### 2.1. Gas density

The medium discussed in the present paper is the cold phase of the neutral ISM, the cold neutral medium (CNM). The thermal pressure of this medium has been measured with observations of the [CI] line by Jenkins & Tripp (2011) to have a mean value  $P_{th}/k_B = 3800 \text{ K cm}^{-3}$ , with most of the gas in the range  $2 \times 10^3$  to  $10^4 \text{ K cm}^{-3}$ . The lower temperature of the CNM is reliably determined from HI absorption measurements  $T_K \gtrsim 80 \text{ K}$ , from which we infer a range of upper limits for the gas densities  $n_H \lesssim 25 \text{ cm}^{-3}$  to  $125 \text{ cm}^{-3}$ . Goldsmith (2013) has computed the excitation temperatures of CO molecules seen through several absorption lines against nearby stars (Sheffer et al. 2008). He infers median values of the density  $n_H = 92 \text{ cm}^{-3}$  and  $68 \text{ cm}^{-3}$  for gas temperatures 50 and 100 K, respectively, and therefore thermal pressures well within the range of Jenkins and Tripp (2011). An independent determination is based on [CII] and [CI] observations of the same sightlines as those where the  $\text{CH}^+(1-0)$  line has been detected (Gerin et al. 2014). Self-absorption of the [CII] line occurs over the same velocity range as that of the  $\text{CH}^+(1-0)$  absorption (see also Falgarone et al. 2010b). The excitation analysis of the [CII] and [CI] lines at these velocities shows that the gas causing the  $\text{CH}^+(1-0)$  absorption is indeed the CNM, with a narrow range of densities from  $n_H = 50 \text{ cm}^{-3}$  to less than  $200 \text{ cm}^{-3}$ .

### 2.2. Gas column densities

For reasons linked to their excitation conditions, most of the molecular lines observed in the diffuse ISM are seen in absorption against continuum sources that are either quasars and free-free emission of HII regions, at millimetre frequencies or warm dust thermal emission in star forming regions, at submillimetre frequencies. One exception is the CO(1-0) line which can be excited in gas densities as low as  $50 \text{ cm}^{-3}$  and provide a detectable level of line emission (Liszt & Pety 2012). The parameters di-

rectly inferred from observations are the line optical depth at a given velocity and the velocity distribution.

Absorption lines corresponding to long pathlengths across the Galaxy have broad line profiles that are usually decomposed into individual Gaussian components. The Gaussian shape, the number of components, and their width are somewhat arbitrary. This is not a major limitation, because the total hydrogen column density (atomic and molecular) with which those of molecular species are associated are computed over the same velocity components found in the profiles of HI for the atomic gas, and CH and HF for  $\text{H}_2$  (e.g. Godard et al. 2012). The column densities plotted in most of the figures of the paper are those associated with these Gaussian velocity components. This is the reason that the plotted total column densities of hydrogen are never much larger than  $10^{22} \text{ cm}^{-2}$ , in spite of the long pathlengths sampled in the Galactic plane by the *Herschel* observations. Whether or not a well-defined “cloud” of gas is ascribed to each of these components is a question that goes beyond the scope of our paper. Following Rachford et al. (2002), we stress that a *translucent line of sight* in the diffuse ISM is definitely different from a *translucent cloud* since large column densities in general result from the accumulation on the same line of sight of a large number of fragments, each of low column density, and presumably poorly shielded from the ambient UV field. This has been well illustrated by Levrier et al. (2012) who show, using numerical simulations of magnetohydrodynamical (MHD) turbulence, that the column density peaks do not correspond to sightlines towards density peaks in the cube.

### 2.3. UV shielding

The very large scatter (by several orders of magnitude) of the  $\text{H}_2$  fraction observed on sightlines with total hydrogen column densities ranging between  $3 \times 10^{19} \text{ cm}^{-2}$  and  $5 \times 10^{20} \text{ cm}^{-2}$  (Gillmon et al. 2006) is also an illustration that the gas on such diffuse sightlines is highly fragmented and that there is not a systematic increase in the UV-shielding with the gas column density sampled. Molecular hydrogen fractions are computed in Appendix B using the Meudon PDR (photodissociation regions) code<sup>1</sup> (Le Petit et al. 2006) for a range of densities and UV-shieldings. The  $\text{H}_2$  self-shielding is so efficient that the sharp transition from  $f_{\text{H}_2} \sim 10^{-4}$  to 0.1 or more always occurs for very low UV-shieldings,  $A_V \lesssim 0.02$  mag, even at a density as low as  $10 \text{ cm}^{-3}$ . This is well below the range of observed UV-shieldings,  $0.02 \lesssim A_V \lesssim 0.3$  mag, that can be inferred from the above range of  $N_H$  assuming  $N_H = 1.8 \times 10^{21} A_V \text{ cm}^{-2}$ . The only way to reconcile what is known on the self-shielding of  $\text{H}_2$  and the observed width of the transition region, given the low densities of the diffuse ISM, is that this column density range is due to tens of fragments of very low column density and probably low UV-shielding as well.

### 2.4. The free parameters linked to turbulence in the diffuse ISM

The CNM is a highly turbulent medium and its supra-thermal kinetic and magnetic pressures provide it with the required support to reach quasi-static equilibrium in the gravitational potential of the Galaxy (Cox 2005). Its weak ionisation degree, carried by  $\text{C}^+$  ions, makes it not fully coupled to the magnetic fields. Turbulence in this cold phase of the interstellar medium is therefore magnetised, compressible, and multifluid, with a high

<sup>1</sup> Version 1.4.4 available at <http://pdr.obspm.fr/PDRcode.html>.

Reynolds number. The power spectra of both the velocity and the column density inferred from HI line emission are found to have the slope of the Kolmogorov incompressible turbulence (e.g. in the North Celestial Loop complex, Miville-Deschênes et al. 2003). The energy transfer rate estimated in the atomic turbulent cascade, is found to be the same as that inferred in the diffuse molecular gas, traced by the optically thick CO(1-0) line emission, suggesting that diffuse molecular and atomic gas are part of the same turbulent cascade (Hennebelle & Falgarone 2012). An interesting feature is the large range of fluctuations for this energy transfer rate: it fluctuates by two orders of magnitudes above and below the average value,  $\bar{\epsilon}_{obs} = 2 \times 10^{-25} \text{ erg cm}^{-3} \text{ s}^{-1}$ , and this is independent of the scale at which these fluctuations are measured. The non-thermal rms velocity dispersion at large scale (between 10 pc and 100 pc) ranges between about  $1 \text{ km s}^{-1}$  and  $8.5 \text{ km s}^{-1}$  from the size-linewidth relation in diffuse molecular gas (Falgarone et al. 2009). The column density-weighted rms velocity of CNM HI Gaussian components in the Solar neighbourhood is  $\sim 7 \text{ km s}^{-1}$  (Heiles & Troland 2003) while the distributions of HI linewidths for the coldest components are  $4.9 \text{ km s}^{-1}$  and  $12 \text{ km s}^{-1}$  at larger scale in the Galaxy (Haud & Kalberla 2007). These quantities may be understood as due to turbulence in the diffuse medium (Kalberla & Kerp 2009; Kim et al. 2013).

### 3. Overview of the TDR model

The model of turbulent dissipation regions (TDR) is built on the property of space-time intermittency of turbulence, i.e. its dissipation is not evenly distributed in space but concentrated in bursts. The purpose of the TDR model is to predict the molecular abundances observed in the diffuse ISM taking into account those transiently formed in the warm non-equilibrium chemistry driven by the bursts of turbulent dissipation, in addition to those formed in the ambient medium, via UV-driven chemistry. The proper description of the dissipation regions of compressible MHD turbulence being far beyond the grasp of even the most powerful direct numerical simulations (Kritsuk et al. 2007), the approach followed in the model is idealised, but relies on three universal properties of turbulence. (i) The bulk of the kinetic energy in compressible turbulence lies in incompressible modes because of the fast energy transfer from compressible to solenoidal modes (Porter et al. 2002; Vestuto et al. 2003; Kritsuk et al. 2010). (ii) A significant fraction of the turbulent energy in incompressible flow experiments is dissipated in coherent dynamical structures, such as vortices (Douady et al. 1991; Nagaoka et al. 2002; Mouri et al. 2007; Mouri & Hori 2009). Similar structures are found in numerical simulations (Moisy & Jiménez 2004; Kritsuk et al. 2007; Uritsky et al. 2010; Momferratos et al. 2014). Their characteristics are set by those of the ambient turbulence (Jimenez 1997; Tanahashi et al. 2004; Mouri & Hori 2009). (iii) Lagrangian intermittency is observed in laboratory flows to be even more pronounced than in Eulerian statistics and Lagrangian accelerations of the fluid cells are influenced by the large scale dynamics (see the review of Arnéodo et al. 2008).

Numerically, the TDR model is a three-step code (Paper I). It first computes the non-equilibrium thermal and chemical Lagrangian evolutions of the gas during the active dissipation stage. Then, after the end of the dissipation burst, the thermal and chemical relaxation of the gas are computed as functions of time. In a third step, the column densities of all the chemical species treated by the code are computed along a random line of sight across the diffuse ISM, taking into account energetic con-

**Table 1.** Parameters of the TDR model. The standard value and the range of explored values are given in Cols. 3 and 4, respectively.

	unit	standard	range	ref
$n_{\text{H}}$	$\text{cm}^{-3}$	50	20 - 300	<i>a</i>
$\chi$		1	0.5 - 10	<i>b</i>
$A_{\text{V}}$	mag	0.4	0.005 - 1	<i>c</i>
$\zeta_{\text{H}_2}$	$\text{s}^{-1}$	$10^{-16}$	$3 \times 10^{-17} - 3 \times 10^{-16}$	<i>d, e</i>
$a$	$\text{s}^{-1}$	$3 \times 10^{-11}$	$10^{-11} - 10^{-10}$	<i>f</i>
$u_{\theta, \text{M}}$	$\text{km s}^{-1}$	3.0	1 - 7	<i>g, h, i</i>
$\bar{\epsilon}$	$\text{erg cm}^{-3} \text{ s}^{-1}$	$10^{-24}$	$10^{-25} - 10^{-23}$	<i>j</i>
$E_{\tau_{\text{V}}}$	$\text{erg cm}^{-1}$	$3 \times 10^{-13}$	$10^{-13} - 10^{-11}$	

(a) Snow & McCall (2006), (b) Mathis et al. (1983), (c) Godard et al. (2012), (d) Dalgarno (2006), (e) Indriolo & McCall (2012), (f) Godard et al. (2009), (g) Tanahashi et al. (2004), (h) Mouri et al. (2007), (i) Mouri & Hori (2009), (j) Hennebelle & Falgarone (2012)

straints. We briefly summarise below the main features of each of these steps, all the details being given in Paper I. The free parameters of the model and the range of values explored in the present work are given in Table 1.

#### 3.1. The active dissipative stage

This stage is treated in a hybrid way. Following the above, we adopt a modified Burgers vortex (Nolan & Farrell 1999) for the coherent structures responsible for intermittent dissipation. Such a vortex results from the balance between the diffusion and the stretching of the vorticity by the rate-of-strain. The vortex is defined by two independent parameters, the maximum orthoradial velocity  $u_{\theta, \text{M}}$  and the turbulent rate-of-strain  $a$  (see Table 1). The vortex equilibrium radius is  $r_0^2 = 4\nu/a$ , where  $\nu$  is the molecular viscosity. We first compute the steady-state equilibrium of such a vortex of finite length threaded by a magnetic field, initially parallel to the vorticity (Mininni et al. 2006b,a). The steady-state configuration is reached within  $\sim 100 \text{ yr}$  with a slightly helical field and ion velocities at least 10 times smaller than  $u_{\theta, \text{M}}$ .

In this configuration, the gas is mechanically heated through viscous friction and ion-neutral friction, at an average rate per unit volume  $\bar{\Gamma}_{\text{turb}}$  computed up to a radius  $Kr_0$  ( $K \sim 5$ , see Paper I) where the turbulent heating stops influencing the gas temperature and chemistry. The gas cools down through atomic and molecular line emissions. The duration of this phase (i.e. the lifetime of the vortex),  $\tau_{\text{V}}$ , is related to the total energy dissipated per unit length of the vortex<sup>2</sup> over its lifetime and volume (hereafter called the vortex dissipation integral),

$$E_{\tau_{\text{V}}} = \pi (Kr_0)^2 \bar{\Gamma}_{\text{turb}} \tau_{\text{V}}, \quad (1)$$

a free parameter also introduced in Paper I. The non-equilibrium coupled thermal and chemical evolutions of the gas are computed along the Lagrangian trajectory of a fluid particle trapped in the vortex. The code simultaneously solves the time-dependent evolution of 11 dynamical and 181 chemical variables, including the abundances of 163 species and of the first 18 rotational levels of  $\text{H}_2$  (see Appendix A). The rates of all col-

<sup>2</sup> The vortex is invariant along its axis.

lisional processes (including chemical reactions) are computed at an effective temperature (Flower et al. 1985),

$$T_{\text{eff}} = \frac{m_1 T_2 + m_2 T_1}{m_1 + m_2} + \frac{1}{k} \frac{m_1 m_2}{m_1 + m_2} u_D^2, \quad (2)$$

where  $m_1$ ,  $m_2$ ,  $T_1$ , and  $T_2$  are the masses and temperatures of the two colliders,  $u_D$  is their relative velocity, and  $k$  is the Boltzmann constant.

### 3.2. The relaxation stage

By nature, an active dissipation burst has a short lifetime  $\tau_V$ . Once it ends, the gas cools down and the chemical signatures imprinted by the active stage persist from a few hundred years to a few  $10^4$  years depending on the destruction timescales of the different species. An Eulerian approach is adopted here: the code computes the chemical and thermal evolutions of 50 points evenly distributed along the radial axis of the vortex, now at rest, assuming that the gas obeys an isochoric or isobaric equation of state. All the results presented in the following are obtained for an isochoric relaxation. The column densities of any species  $X$  integrated across the vortex,  $N_R(X, t)$ , are therefore computed as functions of time.

The relaxation timescales  $\tau_R(X)$  defined as

$$\int_0^{\tau_R(X)} N_R(X, t) dt = 0.9 \int_0^\infty N_R(X, t) dt \quad (3)$$

are shown in Fig. 1 as functions of the shielding of the UV field (left panel) and the density of the gas (right panel) for  $\text{CH}^+$  and four oxygen bearing species,  $\text{OH}$ ,  $\text{H}_2\text{O}$ ,  $\text{HCO}^+$ , and  $\text{CO}$ . This figure illustrates the very large scatter among the chemical relaxation timescales: from a few 100 yr for  $\text{CH}^+$  and  $\text{SH}^+$  to more than  $10^4$  yr for  $\text{CO}$ . Among all the species treated in our chemical network (see Appendix A),  $\text{CO}$  has the largest relaxation timescale as long as  $A_V \gtrsim 0.3$  mag and  $n_{\text{H}} \gtrsim 30 \text{ cm}^{-3}$ . This is due to the shielding of the molecule from the UV radiation field (see Appendix B).

### 3.3. Building of a line of sight

#### 3.3.1. The three phases sampled by a random line of sight

In Fig. 2 we display a schematic view of the turbulent diffuse interstellar medium. In this conception, most of the gas volume is filled by a non-dissipative medium (in green; hereafter called the ambient medium) where the chemical composition of the gas solely results from its density  $n_{\text{H}}$ , the strength  $\chi$  of the UV radiation field (expressed in Mathis' unit, Mathis et al. 1983), the shielding  $A_V$  of the ISRF (at visible wavelength) at each position, and the total CR ionisation rate of molecular hydrogen  $\zeta_{\text{H}_2}$  (taking into account secondary ionisations). In addition to this ambient medium, a random line of sight intercepts a number  $\mathcal{N}_V$  of active vortices (in red) and a number of relaxation stages (in blue). Since each relaxation phase follows an active dissipation phase, their number along the line of sight at any time is proportional to  $\mathcal{N}_V$  and to  $\tau_R(X)/\tau_V$  where  $\tau_R(X)$  is the relaxation timescale of species  $X$ . Introducing the filling factor of the active vortices on a line of sight of length  $L$ ,

$$f_L = \mathcal{N}_V 2Kr_0/L, \quad (4)$$

the column density of a species  $X$  writes<sup>3</sup>

$$N(X) = N_{\text{amb}}(X) + f_L N_V(X) + f_L \frac{\tau_R(X)}{\tau_V} \bar{N}_R(X), \quad (5)$$

where  $N_{\text{amb}}(X)$  is its column density in the ambient medium,  $N_V(X)$  its column density in an active vortex, and  $\bar{N}_R(X)$  its averaged column density during the relaxation phase. We note that according to Fig. 2 (lower panel),  $N_V(X)$  and  $\bar{N}_R(X)$  are computed as excesses<sup>4</sup> of column densities compared to  $N_{\text{amb}}(X)$ . We also note that  $f_L$  being defined on any random line of sight, it corresponds to a volume filling factor. It thus relates the dissipation rate averaged at large scale  $\bar{\epsilon}$  to the same quantity averaged over the volume of a vortex:

$$\bar{\epsilon} = f_L \bar{\Gamma}_{\text{turb}}. \quad (6)$$

Aside from  $n_{\text{H}}$ ,  $\chi$ ,  $A_V$ , and  $\zeta_{\text{H}_2}$ , the TDR model is therefore defined by four independent parameters: the turbulent rate-of-strain  $a$ ; the vortex maximum orthoradial velocity  $u_{\theta, \text{M}}$  (which sets the ion-neutral velocity drift  $v_{\text{in}}$ ); the vortex dissipation integral  $E_{\tau_V}$  (involving the vortex lifetime  $\tau_V$ ); and the average dissipation rate  $\bar{\epsilon}$ , related to the volume filling factor  $f_L$  of all the active vortices.

#### 3.3.2. Prescriptions for the shielding of the UV radiation field

The UV radiation field being a main input of the gas phase chemistry, the prescription for the radiative transfer is critical. In this paper, we adopt two different descriptions of the variation of  $A_V$

<sup>4</sup> These quantities may therefore be negative.

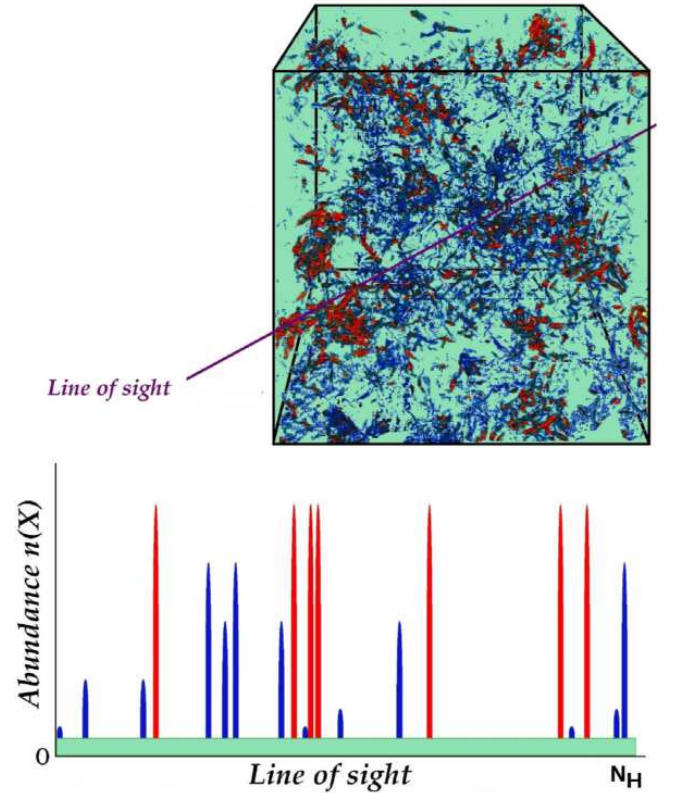


**Figure 2.** Schematic view of the TDR model. A random line of sight across the diffuse interstellar medium intercepts the ambient UV-dominated gas (in green), a number of active vortices (in red), and the corresponding number of relaxation stages (in blue). The chemical enrichment (shown in the lower panel) only occurs on a small fraction of the entire line of sight (a few percent, Paper I).

<sup>3</sup> There is an unfortunate misprint in this Equation in paper I.

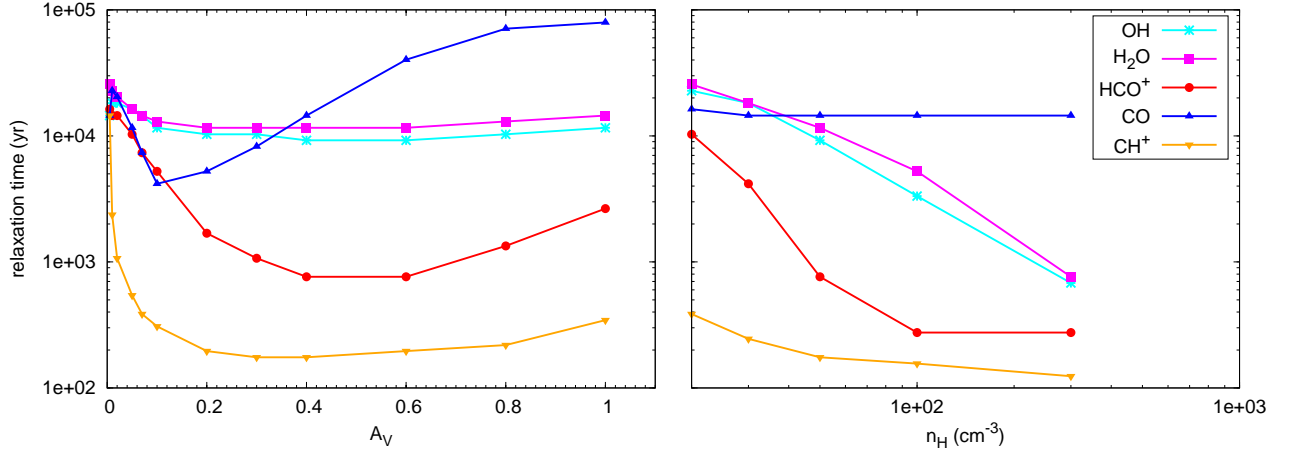


**Figure 1.** Relaxation timescales (Eq. 3) of OH (cyan crosses), H<sub>2</sub>O (magenta squares), HCO<sup>+</sup> (red circles), CO (blue triangles), and CH<sup>+</sup> (orange upside-down triangles) computed with the TDR model as functions of the shielding  $A_V$  of the UV field (left panel) and the density  $n_H$  of the gas (right panel), all the other parameters being set to their standard values (see Table 1).

along the line of sight. In the first approach (standard case), a homogeneous FUV shielding is adopted along the entire line of sight: the medium is considered as highly fragmented, each fragment being evenly shielded by its environment. In the second approach, we mimic PDR models: we consider a 1D slab illuminated from both sides with the same UV radiation field (parametrised by  $\chi$ ) and adopt a shielding function that linearly increases from the edge to the mid plane of the slab and then linearly decreases up to the opposite edge.

In the following, the predictions of the model will always correspond to those obtained with the first approach, except when indicated otherwise.

## 4. Chemical diagnostics of turbulent dissipation

### 4.1. Exploration of the parameter space

The influence of the parameters of the TDR model on the vortex dynamics and lifetime, the thermal evolution of the gas, and the distributions of the active and relaxation phases along the line of sight have been extensively described in Paper I. In the present paper, we broaden the parameter domain explored and focus on their impact on the chemical composition of a random line of sight.

The elemental abundances are set to their values observed in the Solar neighbourhood (SN, see Table A.1 in Appendix A). We explore the parameter domain of the code through a grid of  $\sim 20,000$  models<sup>5</sup> (corresponding to a total computing time of  $\sim 500$  hours) organised as follows:

- 5 densities  $n_H = 20, 30, 50, 100$ , and  $300 \text{ cm}^{-3}$  to bracket the range discussed in Sect. 2;
- 4 radiation field scaling factors  $\chi = 0.5, 1, 3$ , and  $10$ , to take into account variations from the SN to the inner Galactic disk (cf. Sect. 5.4);
- 12 visible extinctions  $A_V = 0.005, 0.01, 0.02, 0.05, 0.07, 0.1, 0.2, 0.3, 0.4, 0.6, 0.8$ , and  $1.0 \text{ mag}$  to explore media with very low UV shielding as discussed in Sect. 2;

<sup>5</sup> Since  $\bar{\epsilon}$  and  $E_{\tau_V}$  are only used for building a line of sight, there is no need to run additional models when we change these parameters.

- 3 cosmic ray ionisation rates  $\zeta_{H_2} = 3 \times 10^{-17}, 10^{-16}$ , and  $3 \times 10^{-16} \text{ s}^{-1}$  to explore the largest average value recently derived in the diffuse ISM (Padovani & Galli 2013; Indriolo & McCall 2012);
- 3 rates-of-strain  $a = 1, 3$ , and  $10 \times 10^{-11} \text{ s}^{-1}$  (Paper I);
- 9 maximum orthoradial velocities  $u_{\theta,M} = 1, 2, 2.5, 3, 3.5, 4, 5, 6$ , and  $7 \text{ km s}^{-1}$  following Sect. 2;
- 5 average dissipation rates  $\bar{\epsilon} = 0.1, 0.3, 1, 3$ , and  $10 \times 10^{-24} \text{ erg cm}^{-3} \text{ s}^{-1}$  following Sect. 2; and
- 5 vortex dissipation integrals  $E_{\tau_V} = 0.1, 0.3, 1, 3$ , and  $10 \times 10^{-12} \text{ erg cm}^{-1}$ , i.e. below the value above which this parameter has no impact (Sect. 7) and keeping only dissipation timescales above the validity limit of the model (see Paper I).

In the paper, we will often refer to a standard model defined by  $n_H = 50 \text{ cm}^{-3}$ ,  $\chi = 1$ ,  $A_V = 0.4 \text{ mag}$ ,  $\zeta_{H_2} = 10^{-16} \text{ s}^{-1}$ ,  $a = 3 \times 10^{-11} \text{ s}^{-1}$ ,  $u_{\theta,M} = 3 \text{ km s}^{-1}$ ,  $\bar{\epsilon} = 10^{-24} \text{ erg cm}^{-3} \text{ s}^{-1}$ , and  $E_{\tau_V} = 3 \times 10^{-13} \text{ erg cm}^{-1}$ . We discuss the influence of  $\zeta_{H_2}$  on the chemistry of the gas and justify our choice for the standard value in Sect. 9.2. Unless indicated otherwise, all the parameters are systematically set to their standard values.

### 4.2. Method: ternary phase diagrams

A helpful way to visualise the main results of the TDR model are the ternary phase diagrams shown in Fig. 3. They display schematic representations of the contributions (see Eq. 5)

$$f_{\text{amb}}(X) = N_{\text{amb}}(X)/N(X) \quad (7)$$

$$f_V(X) = \mathcal{N}_V N_V(X)/N(X) \quad (8)$$

$$f_R(X) = \mathcal{N}_V \frac{\tau_R(X)}{\tau_V} \bar{N}_R(X)/N(X) \quad (9)$$

of the ambient medium, the active vortices, and the relaxation stages to the total column densities of ten molecules. These contributions are given by the projections of each point on the three triangle axis: for instance, the smallest symbol of CO (top left panel) reads  $f_{\text{amb}}(\text{CO}) = 22 \%$ ,  $f_V(\text{CO}) = 21 \%$ , and  $f_R(\text{CO}) = 57 \%$ . These diagrams illustrate two major features of the model.



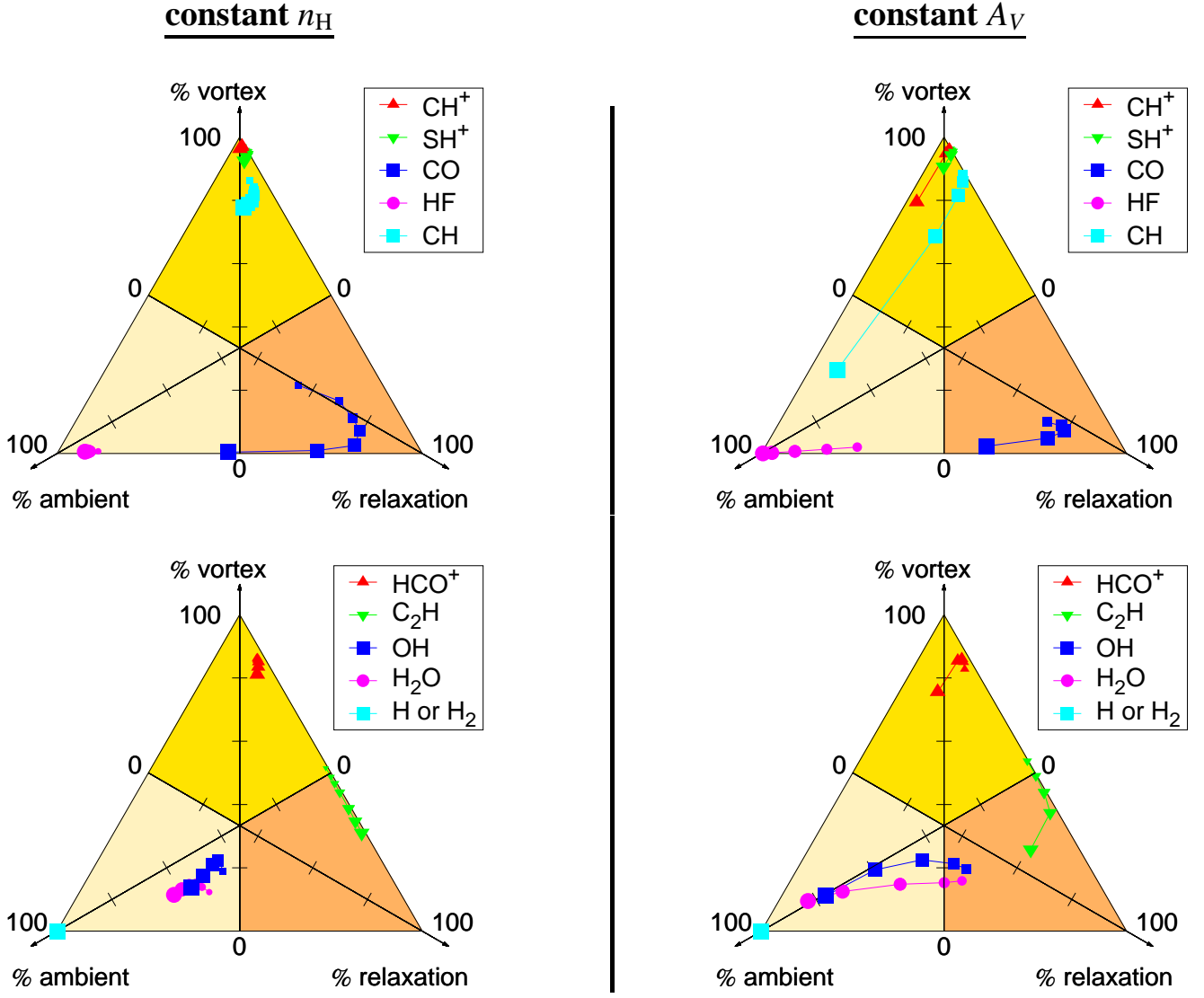


**Figure 3.** Ternary phase diagram of the TDR model. The projections of each point on the medians of the equilateral triangle show the contributions of each phase (ambient medium, active dissipative bursts, and relaxation stages) to the total column density of a given species. In the left panels, the models are computed for several values of  $A_V$ : 0.1, 0.2, 0.3, 0.4, 0.6, 0.8, and 1.0 mag. In the right panels, the models are computed for several values of  $n_H$ : 20, 30, 50, 100, and 300  $\text{cm}^{-3}$ . All the other parameters are set to their standard values (see Table 1). In all panels, the size of the symbols increases as the varying parameter increases. The beige, yellow, and orange zones indicate the regions where the production of the different species is dominated by the ambient medium, the active vortices, and the relaxation stages, respectively.

First, the phase contributions of the species selected here are distributed over the entire area of the triangles. It implies that each phase of the TDR model plays a role on the global chemical composition of the gas, even if it fills only a small fraction of the entire volume, and is therefore required to correctly model random diffuse lines of sight. In particular, Fig. 3 shows for the first time the critical impact of the relaxation times: the relaxation phase may account for 15 % of the total column density of CH, 50 % of those of OH and  $\text{H}_2\text{O}$ , 70 % of  $\text{C}_2\text{H}$ , and for more than 80 % of the total column density of CO.

Second, except for CH, the production of which is dominated by the active phase at low density and by the ambient medium as the density increases, and for OH and  $\text{H}_2\text{O}$ , the productions of which may be dominated by the relaxation phase at low density, all the other species appear to be confined in specific regions of the triangles: H,  $\text{H}_2$ , and HF are almost entirely produced

in the ambient medium;  $\text{SH}^+$ ,  $\text{CH}^+$ , and  $\text{HCO}^+$  are predominantly formed in the active phase; while  $\text{C}_2\text{H}$  and CO mostly originate from the relaxation phase. We therefore anticipate that the species produced in the active phase can be used as signatures of the dynamics of the dissipation regions; those formed in the relaxation phase are expected to be sensitive to the relative timescales between the active dissipation and the relaxation; and those produced in the ambient medium are species unaffected by turbulent dissipation.

In the next sections, we select several pairs of species and compare both their column densities and column density ratios predicted by the TDR model to the observations of hundreds of diffuse lines of sight. The goal of this approach is to address the following questions: How do the model predictions compare with multiwavelength observations of atoms and molecules in the diffuse medium across the Galactic disk? Conversely, how

can we use these observations to constrain the parameter space, hence infer the main properties of turbulent dissipation?

## 5. CH<sup>+</sup> and the turbulent dissipation rate

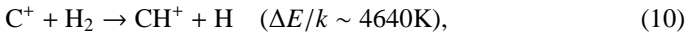
### 5.1. Observational data

In the top panel of Fig. 4 we compare two datasets: the column densities of CH<sup>+</sup> derived from its visible absorption lines (in red) detected towards nearby OB stars (Crane et al. 1995; Gredel 1997; Weselak et al. 2008) and those deduced from its far-infrared rotational transitions (in blue) recently observed in absorption towards the continuum of massive star forming regions with the *Herschel*/HIFI instrument (Falgarone et al. 2010a; Godard et al. 2012). The total hydrogen column densities associated with the visible data are inferred from extinction measurements, while those associated with the far-infrared data are taken from Godard et al. (2012) who estimated the atomic hydrogen column density from VLA observations of its  $\lambda 21$  cm transition and the H<sub>2</sub> column density from the far-infrared observations of two surrogate molecular species, CH and HF (Gerin et al. 2010b; Neufeld et al. 2010b; Sonnentrucker et al. 2010). When both CH and HF are available, both estimations are used to compute uncertainties on the total column density, hence the large error bars on  $N_{\text{H}}$  for several far-infrared components.

Absorption spectroscopy against stars in the visible range is limited to the SN because of dust extinction, while that against star-forming regions in the submillimetre domain does not have such a limitation (e.g. Laor & Draine 1993). The red data of Fig. 4 are thus associated with gas in the SN while the blue data sample components located deeper in the inner Galactic disk (see Table 3 of Godard et al. 2012). These two datasets share similar characteristics: a large scatter of about one order of magnitude and the same linear trend with  $N_{\text{H}}$ . However, the column densities of CH<sup>+</sup> observed in the inner Galactic disk, with a mean ratio  $\langle N(\text{CH}^+)/N_{\text{H}} \rangle = 2.1 \times 10^{-8}$ , are found to exceed by a factor of 3 on average those observed in the SN, where  $\langle N(\text{CH}^+)/N_{\text{H}} \rangle = 7.6 \times 10^{-9}$ .

### 5.2. Predictions of UV-dominated chemistry

The middle panel of Fig. 4 displays the column densities of CH<sup>+</sup> predicted by the Meudon PDR code for densities of 30, 50, and 100 cm<sup>-3</sup>, a total column density  $N_{\text{H}} = 0.18, 1.8,$  and  $18 \times 10^{21}$  cm<sup>-2</sup>, and an incident radiation field scaling factor  $\chi = 1$ . In the diffuse ISM, the destruction of CH<sup>+</sup> occurs through hydrogenation (see Fig. C.1 in Appendix C), an exothermic process with a very short timescale  $\sim 1 \text{ yr } f_{\text{H}_2} (50 \text{ cm}^{-3}/n_{\text{H}})$  (McEwan et al. 1999), where  $f_{\text{H}_2}$  is the molecular fraction defined as  $f_{\text{H}_2} = 2n(\text{H}_2)/n_{\text{H}}$ . Conversely, in the absence of a suprathermal energy source to activate the endothermic reaction



the formation of CH<sup>+</sup> is initiated by the radiative association



a process with a very long timescale  $\sim 2 \times 10^6 \text{ yr } f_{\text{H}_2}^{-1} (50 \text{ cm}^{-3}/n_{\text{H}})$  (Herbst 1985). With the lack of an efficient production pathway, PDR models thus systematically underestimate the observed column densities of CH<sup>+</sup> by one to three orders of magnitude (Fig. 4).

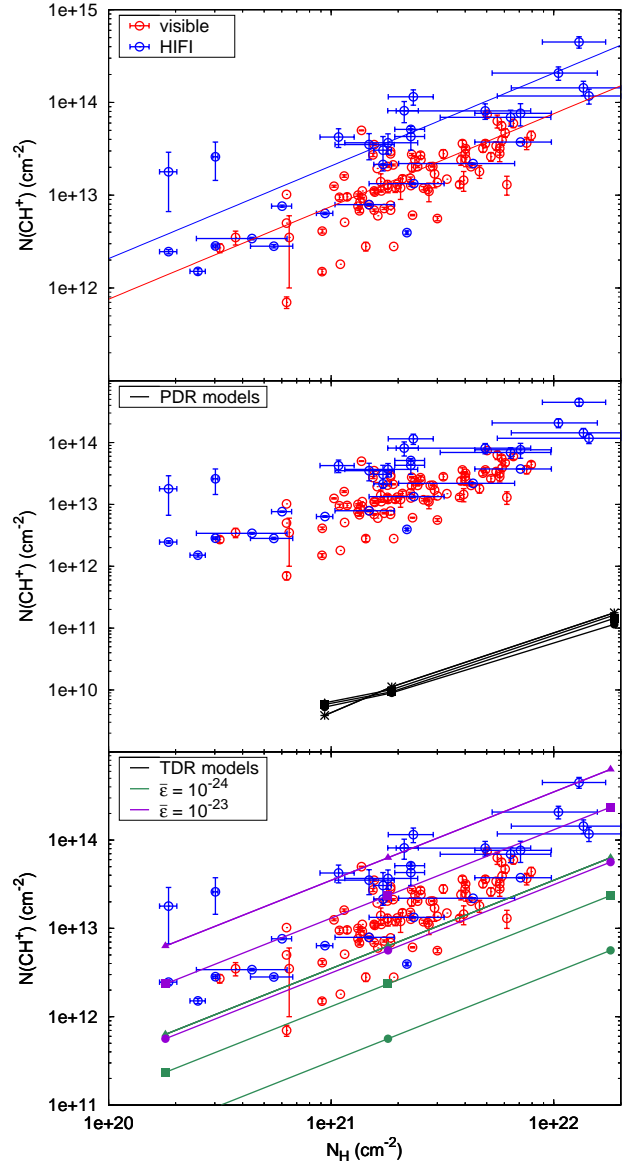


**Figure 4.** Observations (*top panel*) compared to the predictions of PDR (*middle panel*) and TDR (*bottom panel*) models. Data (open circles) – The CH<sup>+</sup> and total hydrogen column densities inferred from visible absorption lines and extinction measurements are shown in red and are from Crane et al. (1995), Gredel (1997), and Weselak et al. (2008). The CH<sup>+</sup> and total hydrogen column densities inferred from the far-infrared absorption lines of CH<sup>+</sup>, HF, and CH and the 21 cm emission lines of HI are shown in blue and are from Falgarone et al. (2010a), Gerin et al. (2010b), Neufeld et al. (2010b), Sonnentrucker et al. (2010), and Godard et al. (2012). The red and blue lines correspond to the mean ratio  $N(\text{CH}^+)/N_{\text{H}}$  computed with the visible and submillimetre data, respectively. PDR and TDR model predictions (filled symbols) – Computed for several densities: 10 (crosses), 30 (triangles), 50 (squares), and 100 cm<sup>-3</sup> (circles). The TDR models are computed for  $\bar{\epsilon} = 10^{-24}$  (green) and  $10^{-23}$  (magenta) erg cm<sup>-3</sup> s<sup>-1</sup>, all the other parameters are set to their standard values.

### 5.3. Predictions of the TDR model

In the bottom panel of Fig. 4, we compare the observational data with the predictions of the TDR models. With a homogeneous reconstruction of the line of sight (see Sect. 3.3), all the column densities computed by the code are simply proportional to the total hydrogen column density  $N_{\text{H}}$ . For a given  $N_{\text{H}}$ , the dependence of  $N(\text{CH}^+)$  on the other parameters is then the result of several effects. First,  $\text{CH}^+$  is predominantly produced in the active stages (see Fig. 3); its column density is thus proportional to the number of active vortices, which is proportional to the average dissipation rate  $\bar{\epsilon}$ , inversely proportional to the square of the density  $n_{\text{H}}$  and independent of  $E_{\text{TV}}$  (see Paper I). Second, the rate-of-strain  $a$  and the maximum orthoradial velocity  $u_{\theta, \text{M}}$  control the heating by viscous friction and ion-neutral friction, respectively, hence set the effective temperature (Eq. 2) at which ion-neutral chemical reactions proceed. If  $a$  or  $u_{\theta, \text{M}}$  increase, the effective temperature in an active vortex increases and so does the rate of reaction 10, hence the production of  $\text{CH}^+$ . When integrated over the line of sight, however, this effect is balanced by the number of vortices which decreases as the local dissipation rate increases (Paper I). Third, since  $\text{CH}^+$  is formed through the hydrogenation of  $\text{C}^+$  and the photodissociation of  $\text{CH}_3^+$  (see Fig. C.1 of Appendix C), its abundance, unlike most of the molecules, increases with the UV radiation field. With the analysis of all the models we find that the  $N(\text{CH}^+)/N_{\text{H}}$  column density ratio scales as

$$N(\text{CH}^+)/N_{\text{H}} \sim 1.5 \times 10^{-9} \bar{\epsilon}_{24} \left( \frac{n_{\text{H}}}{50 \text{ cm}^{-3}} \right)^{-2.2} \left( \frac{A_{\text{V}}}{0.4 \text{ mag}} \right)^{-0.3} \chi^{0.5} \quad (12)$$

(with  $\bar{\epsilon}_{24} = 10^{24} \bar{\epsilon} \text{ erg cm}^{-3} \text{ s}^{-1}$ ) for  $n_{\text{H}} \lesssim 300 \text{ cm}^{-3}$ , and is almost independent of  $u_{\theta, \text{M}}$  for  $u_{\theta, \text{M}} \gtrsim 2.5 \text{ km s}^{-1}$ , i.e. as long as the gas rotation induces a sufficient ion-neutral drift to activate reaction 10.

The above relation shows a weak dependence of  $N(\text{CH}^+)$  on both  $A_{\text{V}}$  and  $\chi$ ;  $N(\text{CH}^+)$  varies by only a factor of 3 over the ranges covered by these two parameters which are inferred from the molecular fractions of the gas (see Sect. 2) and from its positions in the Galactic disk (see Sect. 5.4). Equation 12 reveals stronger dependences of  $N(\text{CH}^+)$  on both  $\bar{\epsilon}$  and  $n_{\text{H}}$ , the latter reflecting the fast destruction of  $\text{CH}^+$  by collisions with hydrogen. This result somewhat hampers the interpretation of the observations: (1) there is a degeneracy between  $\bar{\epsilon}$  and  $n_{\text{H}}$  from the sole observations of  $N(\text{CH}^+)$  and  $N_{\text{H}}$  and (2) the steep dependence on  $n_{\text{H}}$  implies that the observations of  $\text{CH}^+$  preferentially sample the lowest densities of the diffuse medium.

The lowest values of  $N(\text{CH}^+)/N_{\text{H}}$  in Fig. 4 correspond to detection limits and thus cannot be used to infer a lower limit on the dissipation rate  $\bar{\epsilon}$  or an upper limit on the gas density. In contrast, we can derive an upper limit of the turbulent dissipation rate from the largest observed  $\text{CH}^+$  abundances. The largest values of  $N(\text{CH}^+)/N_{\text{H}}$  observed in the local ISM (red points in Fig. 4) and the inner Galactic disk (blue points in Fig. 4) give  $\bar{\epsilon}_{24} \times (n_{\text{H}}/50 \text{ cm}^{-3})^{-2.2} \lesssim 20$  and 70, respectively. Assuming that these upper limits are associated with the lowest density components of the diffuse matter ( $n_{\text{H}} \sim 20 \text{ cm}^{-3}$ , Fitzpatrick & Spitzer 1997, see also Sect. 2), we find  $\bar{\epsilon} \lesssim 10^{-23} \text{ erg cm}^{-3} \text{ s}^{-1}$  for the components located in the inner Galactic disk, and about 3 times less in the SN.

### 5.4. Variation of $N(\text{CH}^+)/N_{\text{H}}$ across the Galactic disk

It is interesting to analyse the increase by a factor of three of the  $\text{CH}^+$  abundance between the SN and the inner Galaxy in

the light of what is known about the Galactic dynamics and the star formation rate. Although the far-infrared lines of sight intercept the spiral arms of the Galaxy, we assume that, even in the inner Galaxy, the density of the gas rich in  $\text{CH}^+$  remains low because of the fast destruction rate of  $\text{CH}^+$  by collisions. The increase in the carbon elemental abundance towards the inner Galaxy accounts for an increase in the  $\text{CH}^+$  column density by only a factor of 1.2 at  $R_{\text{g}} = 6.5 \text{ kpc}$  because the trend is only of  $0.037 \text{ dex kpc}^{-1}$  (Daflon & Cunha 2004). The increase in the mean ISRF intensity towards the inner Galaxy has an influence (Porter & Strong 2005). Using the SKY star distribution model (Wainscoat et al. 1992), Moskalenko et al. (2006) estimate that the mean UV radiation field intensity increases by a factor of three from  $R_{\text{g}} = 8.5$  to 4 kpc. This sole increase, however, seems insufficient to explain the observed variation of the  $N(\text{CH}^+)/N_{\text{H}}$  ratio because most of the observed components beyond the SN lie in the range  $5.5 - 7.5 \text{ kpc}$  (Godard et al. 2012). What is left is an increase in the turbulent dissipation rate  $\bar{\epsilon}$  that follows the turbulent injection rate. The latter scales with the supernovae explosion rate and the differential rotation of the Galaxy. These two processes are expected to increase  $\bar{\epsilon}$  by a factor of 2.2 (Lumsden et al. 2013; Urquhart et al. 2014) and 1.7 (assuming a flat Galactic rotation curve, Fich & Tremaine 1991) from  $R_{\text{g}} = 8.5 \text{ kpc}$  to  $R_{\text{g}} = 6.5 \text{ kpc}$ . The increase in both the mean UV ISRF and the turbulent energy injection rate are therefore likely to be at the origin of the increase in the  $N(\text{CH}^+)/N_{\text{H}}$  ratio from the SN to the inner Galaxy.

## 6. The $\text{CH}^+$ to $\text{SH}^+$ ratio and the ion-neutral velocity drift

We now select two species mainly formed in the active phases of the TDR model:  $\text{CH}^+$  and  $\text{SH}^+$  (see Fig. 3).

### 6.1. Observational data

As the first step of the sulfur hydrogenation chain, the sulfanylium ion  $\text{SH}^+$  has long been sought without success in the local diffuse ISM through UV absorption spectroscopy of its electronic transitions (Millar & Hobbs 1988; Magnani & Salzer 1989, 1991). Only recently, thanks to the development of submillimetre and infrared telescopes (APEX, *Herschel*), has interstellar  $\text{SH}^+$  finally been observed through its ground-state rotational transitions (Menten et al. 2011; Godard et al. 2012; Nagy et al. 2013). Among these new data, those of Godard et al. (2012) are particularly interesting because they show the first unambiguous detection of  $\text{SH}^+$  in diffuse interstellar components. As illustrated by the top panel of Fig. 5, the  $\text{SH}^+/\text{CH}^+$  abundance ratio measured in the diffuse gas covers a broad range of values from less than 0.01 to more than 0.1 and appears to be proportional to  $(N(\text{CH}^+)/N_{\text{H}})^{-1.4}$ . In this section we discuss the implications of this relation in the framework of UV-dominated and turbulence-dominated chemistries.

### 6.2. Sulfur chemistry

In many ways, the analysis of the sulfur hydrides provides unique constraints on chemical models applied to the interstellar medium. As quoted by Neufeld et al. (2012), the sulfur differentiates itself from any other abundant element because its hydrides and hydride cations have small bonding energies. In consequence, the chemical reactions  $\text{X} + \text{H}_2 \rightarrow \text{XH} + \text{H}$  are highly endothermic for  $\text{X} = \text{S}, \text{SH}, \text{S}^+, \text{SH}^+$ , and  $\text{SH}_2^+$ . The hydrogenation



tion chain of sulfur therefore displays very distinctive chemical

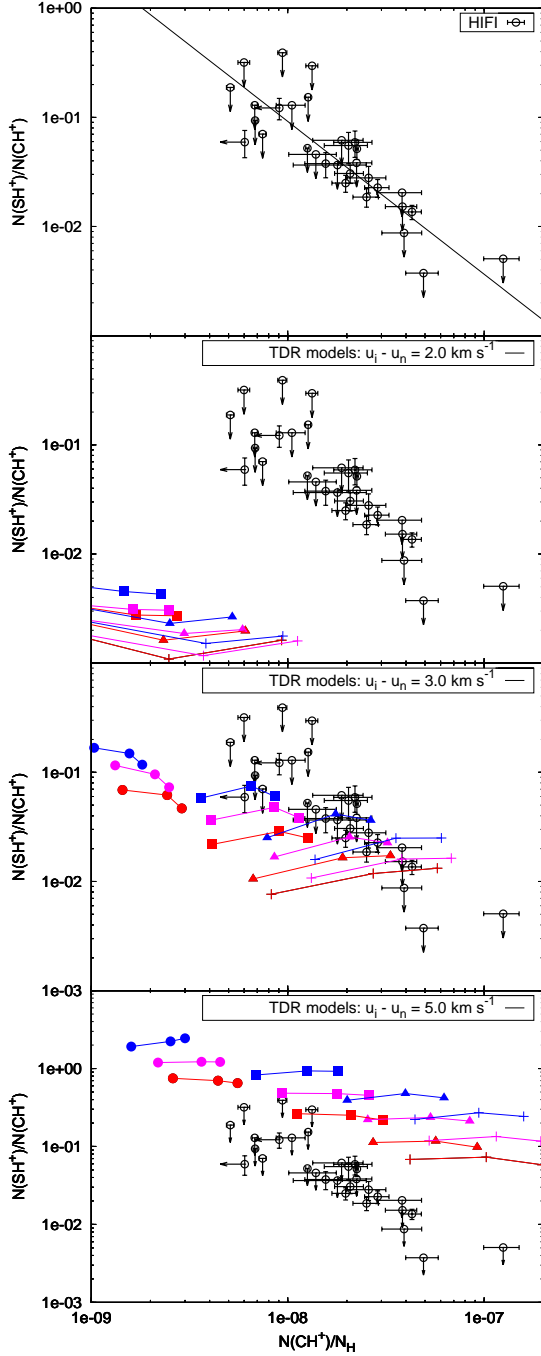


**Figure 5.** Observations (*top panel*) compared to the predictions of TDR models computed for three values of the maximum ion-neutral velocity drift: starting from the second panel,  $u_i - u_n = 2.0, 3.0$ , and  $5.0 \text{ km s}^{-1}$ . Data (open circles) – The  $\text{CH}^+$  and  $\text{SH}^+$  column densities and the least-squares power-law fit of their ratio (black line) are from Godard et al. (2012). Model predictions (filled symbols) – Computed for  $A_V = 0.1$  (red),  $0.2$  (magenta), and  $0.4$  (blue) mag and for several densities:  $20$  (crosses),  $30$  (triangles),  $50$  (squares), and  $100 \text{ cm}^{-3}$  (circles). Along each curve, the rate-of-strain  $a$  varies between  $10^{-11}$  and  $10^{-10} \text{ s}^{-1}$  from right to left.

patterns when compared with that of carbon, both in a UV-driven and turbulence-driven regimes (see Fig. C.1 in Appendix C)

In a UV-driven chemistry, the sulfur hydrogenation is quenched by two reactions:



With their very long characteristic timescales, these two reactions limit the production of  $\text{SH}$  and, by extension, the production of  $\text{SH}^+$  that originates from the photodissociation of  $\text{SH}_2^+$  rather than the photoionisation of  $\text{SH}$ . In addition, and unlike  $\text{CH}^+$  and  $\text{CH}_2^+$  which are destroyed by exothermic reactions with  $\text{H}_2$ , the destructions of  $\text{SH}^+$  and  $\text{SH}_2^+$  mainly occur through

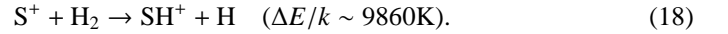


At equilibrium the  $\text{SH}^+/\text{CH}^+$  abundance ratio writes

$$\frac{n(\text{SH}^+)}{n(\text{CH}^+)} \propto \frac{n(\text{S}^+)}{n(\text{C}^+)} \frac{n(\text{H}_2)^2}{n_e^2} \quad (17)$$

and is independent from the extinction  $A_V$  as long as  $\text{C}^+$  and  $\text{S}^+$  are the main ion carriers and the major reservoirs of carbon and sulfur. It results that the  $\text{SH}^+/\text{CH}^+$  column density ratio integrated over PDR slabs is constant for a total extinction varying between  $0.5$  and  $3$  magnitudes and densities varying between  $30 \text{ cm}^{-3}$  and  $500 \text{ cm}^{-3}$ . This ratio is equal to  $0.01$  (Godard et al. 2012), i.e. between one and two orders of magnitude smaller than the largest observed value.

In a chemistry driven by turbulence, the release of energy due to dissipation is sufficient to activate the endothermic reactions producing the sulfur hydride cations such as



The associated timescales decrease and become smaller than those of reactions 13 and 14, yet still larger than those of reactions 15 and 16. Hydrogenation reactions therefore dominate the productions of  $\text{SH}^+$ ,  $\text{SH}_2^+$ , and  $\text{SH}_3^+$ , while their destruction remain driven by the dissociative recombinations. From this simple scheme (see Fig. C.1 in Appendix C), and using the endothermicities given in Eqs. 10 and 18, the  $\text{SH}^+/\text{CH}^+$  abundance ratio writes

$$\frac{n(\text{SH}^+)}{n(\text{CH}^+)} \propto \frac{n(\text{S}^+)}{n(\text{C}^+)} \frac{n(\text{H}_2)}{n_e} \exp\left(-\frac{5220\text{K}}{T_{\text{eff}}}\right) \quad (19)$$

at chemical equilibrium. It follows that  $n(\text{SH}^+)/n(\text{CH}^+)$  strongly depends on the effective temperature  $T_{\text{eff}}$  of reactions 10 and 18, thus on the velocity drift between  $\text{C}^+$  (or  $\text{S}^+$ ) and the molecular hydrogen (see Eq. 2).

### 6.3. Influence of the TDR model parameters

The three bottom panels of Fig. 5 display a comparison between the observational data and the predictions of the TDR models computed for  $u_{\theta,M} = 2, 3$ , and  $5 \text{ km s}^{-1}$ , a density ranging from  $20 \text{ cm}^{-3}$  to  $100 \text{ cm}^{-3}$ , a shielding varying between  $0.1$  mag and  $0.4$  mag, and a total dissipation rate  $\bar{\epsilon} = 3 \times 10^{-24} \text{ erg cm}^{-3} \text{ s}^{-1}$ , i.e. within the range of values deduced in the diffuse ISM from the  $N(\text{CH}^+)/N_{\text{H}}$  ratio (cf. Sect. 5.3).

As expected from the large difference between the  $\text{CH}^+$  and  $\text{SH}^+$  endothermicities, the  $N(\text{SH}^+)/N(\text{CH}^+)$  column density ratio computed with the code is highly sensitive to the ion-neutral velocity drift set by the  $u_{\theta,M}$  parameter. An increase in  $u_{\theta,M}$  by a factor of two induces a rise of  $N(\text{SH}^+)/N(\text{CH}^+)$  from one to three orders of magnitude. Detection limits on  $N(\text{SH}^+)$  prevent us from deriving lower limits on  $u_{\theta,M}$ . In contrast, we infer  $u_{\theta,M} \lesssim 3.5 \text{ km s}^{-1}$  regardless of  $n_{\text{H}}$  and  $A_V$ . For  $u_{\theta,M} = 3 \text{ km s}^{-1}$ , the code not only explains the most extreme values of the  $N(\text{SH}^+)/N(\text{CH}^+)$  column density ratio, but also naturally reproduces its trend with  $N(\text{CH}^+)/N_{\text{H}}$ . The dependence of  $N(\text{CH}^+)$  and  $N(\text{SH}^+)$  on the other parameters indicates that the matter traced by both  $\text{CH}^+$  and  $\text{SH}^+$  has a density  $n_{\text{H}} \lesssim 50 \text{ cm}^{-3}$  in agreement with the results of the previous section.

## 7. The CO to $\text{HCO}^+$ ratio and the dissipation timescale

We now focus on  $\text{HCO}^+$  and CO, i.e. on two species which, according to the ternary phase diagrams (Fig. 3), originate from the active and relaxation stages, respectively. Because these two species are closely related by their chemistry and belong to two different phases of the TDR model, they offer a unique opportunity to obtain information on the relative value of the relaxation and active dissipation timescales.

### 7.1. Observational data

Two different data sets are used: (1) the  $\text{HCO}^+(1-0)$  and  $\text{CO}(1-0)$  lines observed in absorption on the continuum of quasars (Lucas & Liszt 1996; Liszt & Lucas 1998, 2004) and (2) the CO and  $\text{H}_2$  lines observed in the visible and UV ranges in absorption towards nearby OB stars (e.g. Burgh et al. 2007; Sheffer et al. 2008).

In the first set of data (Fig. 6), the selected lines of sight sample all Galactic latitudes (Liszt et al. 2010, Appendix). The observed column densities of CO and  $\text{HCO}^+$  show a non-linear correlation  $N(\text{CO}) \propto N(\text{HCO}^+)^{1.4}$  with an averaged abundance ratio varying between  $5 \times 10^2$  and  $8 \times 10^3$ . The total column densities associated with each data point are similar and close to one magnitude of matter (Paper I).

In the second set of data, displayed in the top panel of Fig. 7, the sightlines sample diffuse components located in the SN, i.e. within  $\sim 1 \text{ kpc}$  from the sun. No correlation is observed between  $N(\text{CO})$  and  $N(\text{H}_2)$ . Unlike in the previous data set, the (unknown) total hydrogen column density associated with the CO data likely spans a large range, not only because the  $\text{H}_2$  column densities vary by two orders of magnitude, but also because the  $\text{H}_2$  fraction is expected to fluctuate by a large factor (Sect. 2).

### 7.2. Oxygen chemistry

In diffuse interstellar gas, CO is expected to be destroyed by photodissociation and formed by the dissociative recombination of  $\text{HCO}^+$ , regardless of turbulent dissipation (see Fig. C.2 of Appendix C). At chemical equilibrium, the CO/ $\text{HCO}^+$  abundance ratio writes

$$\frac{n(\text{CO})}{n(\text{HCO}^+)} = \frac{n_e k_e}{k_\gamma}, \quad (20)$$

where  $k_e = 2.46 \times 10^{-7} (T/300 \text{ K})^{-0.69} \text{ cm}^3 \text{ s}^{-1}$  (Florescu-Mitchell & Mitchell 2006). Adopting the pho-

todissociation rate  $k_\gamma$  (in  $\text{s}^{-1}$ ) of CO given in Fig. B.2 (Appendix B),  $n(\text{CO})/n(\text{HCO}^+)$  is found to vary between  $10^2$  and  $10^5$  for typical diffuse gas conditions ( $30 \lesssim n_{\text{H}} \lesssim 300 \text{ cm}^{-3}$ ,  $0.01 \lesssim A_V \lesssim 1 \text{ mag}$ ), i.e. to entirely cover the observed range (Fig. 6). Consequently, any model computing the chemical equilibrium of the gas should be able to explain the observed abundance of CO, provided that it produces enough  $\text{HCO}^+$ .

In a UV-dominated chemical scheme (see Fig. C.2 of Appendix C), the formation of  $\text{HCO}^+$  proceeds through the oxygen hydrogenation chain followed by the two reactions:  $\text{OH} + \text{C}^+ \rightarrow \text{CO}^+ + \text{H}$  and  $\text{H}_2\text{O} + \text{C}^+ \rightarrow \text{HCO}^+ + \text{H}$ . The bottleneck process of this pathway is the conversion of O into  $\text{O}^+$  via the charge exchange with ionised hydrogen. The abundance of  $\text{HCO}^+$  therefore depends on that of  $\text{H}^+$ , the production of which is driven by the cosmic ray ionisation of H and  $\text{H}_2$ . To investigate this effect, we have run the Meudon PDR code along the grid presented in Appendix B assuming two values of the cosmic ray ionisation rate of molecular hydrogen:  $\zeta_{\text{H}_2} = 3$  and  $30 \times 10^{-17} \text{ s}^{-1}$ . In all cases, and despite the strong dependence of  $n(\text{HCO}^+)$  on  $\zeta_{\text{H}_2}$ , we find that the PDR models systematically underestimate the column densities of  $\text{HCO}^+$  by more than one order of magnitude for  $\zeta_{\text{H}_2} = 3 \times 10^{-17} \text{ s}^{-1}$  and by more than a factor of 5 for  $\zeta_{\text{H}_2} = 3 \times 10^{-16} \text{ s}^{-1}$ . These results are in line with those of Paper I and Levrier et al. (2012) who found similar discrepancies by comparing the predictions of the Meudon PDR code with the observed column densities of CO.

In an active vortex (bottom panel of Fig. C.2 of Appendix C) it is not the hydrogenation chain of O that matters, but that of C. Indeed it enhances the production of the very reactive cation,  $\text{CH}_3^+$ , which swiftly reacts with O to form  $\text{CO}^+$  and  $\text{HCO}^+$ . With the opening of this additional formation pathway, the abundance of  $\text{HCO}^+$  rises by several orders of magnitude and that of CO by a factor of up to 100 (see Fig. 3 of Paper I). If these behaviors appear to be in contradiction with Eq. 20, it is because in dissipative regions the chemistry is not at equilibrium and the electronic fraction is substantially smaller than that in the ambient gas. After integration over the entire line of sight, we showed in Paper I that the sole contributions of the active phases could explain the observed column densities of  $\text{HCO}^+$  for small values of the rate-of-strain  $10^{-11} \lesssim a \lesssim 10^{-10} \text{ s}^{-1}$ , but fail to reproduce those of CO by more than one order of magnitude. Because  $\text{HCO}^+$  and CO only differ by the timescales associated with their respective destruction processes, we suggested in Paper I that CO may in fact trace the relaxation period of turbulent dissipation (Fig. 3).

### 7.3. Influence of the TDR model parameters

To illustrate the influence of the relaxation period for CO, we display the column densities of several species computed across the diameter of a single vortex as functions of time in the left panels of Fig. 6. All parameters are set to their standard values except for  $E_{\tau_V}$  which is set to  $1.4 \times 10^{-11} \text{ erg cm}^{-1}$  (top panels) and  $1.4 \times 10^{-13} \text{ erg cm}^{-1}$  (bottom panels). The corresponding values of the vortex lifetime (see Eq. 1) are indicated by straight vertical lines. Because the vortex is stationary, the column densities it produces are constant over its entire lifetime ( $t \leq \tau_V$ ). Once the vortex has destabilised ( $t > \tau_V$ ), the column density of each species decreases towards that produced by the equivalent amount of matter of ambient gas with a characteristic timescale that depends on the species.

Since the computed column density of a given species takes its time-dependent decrease into account during the relaxation

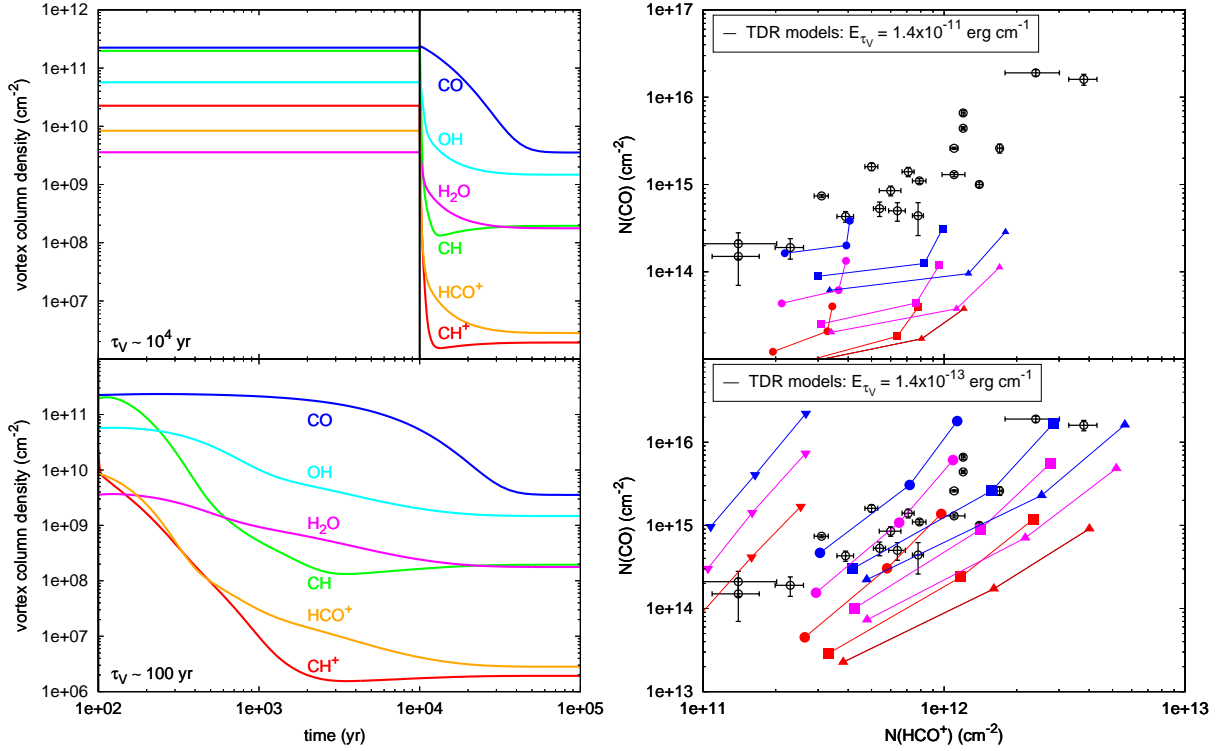


**Figure 6.** *Left panels:* column densities of selected species integrated across a single vortex as functions of time during the isochoric relaxation phase. The models are computed for two values of the vortex dissipation integral  $E_{\tau_V} = 1.4 \times 10^{-11}$  erg cm $^{-1}$  (*top panels*) and  $E_{\tau_V} = 1.4 \times 10^{-13}$  erg cm $^{-1}$  (*bottom panels*). The corresponding vortex lifetimes are indicated with vertical straight lines. All the other parameters are set to their standard values. *Right panels:* comparison of observations with the predictions of TDR models. The observed CO and HCO $^+$  column densities (open circles) are from Lucas & Liszt (1996); Liszt & Lucas (1998, 2004). The predictions of the TDR models (filled symbols) are shown for  $A_V = 0.2$  (red), 0.4 (magenta), and 0.8 (blue) mag,  $n_H = 30$  (triangles),  $n_H = 50$  (squares),  $n_H = 100$  (circles), and  $n_H = 300$  cm $^{-3}$  (upside-down triangles), and a total column density  $N_H = 1.8 \times 10^{21}$  cm $^{-2}$ ; along each curve, the rate-of-strain  $a$  varies between  $10^{-11}$  (right) and  $10^{-10}$  s $^{-1}$  (left).

phase (Eq. 5), Fig. 6 illustrates the importance of the relative values of the active and relaxation phases and their dependence on the vortex dissipation integral  $E_{\tau_V}$ . For large values,  $E_{\tau_V} = 1.4 \times 10^{-11}$  erg cm $^{-1}$ , i.e. large values of  $\tau_V$ , the relaxation phase has no impact on the time-averaged column density of any species. For small values,  $E_{\tau_V} = 1.4 \times 10^{-13}$  erg cm $^{-1}$ , i.e. small values of  $\tau_V$ , the relaxation phase dominates the time-averaged column densities of CO, OH, and H $_2$ O, and may start to have an impact on those of HCO $^+$  and CH.

The resulting total column densities of CO and HCO $^+$  are displayed in the right panels of Fig. 6. We find that the TDR model can account for the observed ranges of column densities of both CO and HCO $^+$  if  $E_{\tau_V}$  is sufficiently small because  $E_{\tau_V}$  affects CO and HCO $^+$  in different ways:  $N(\text{CO})$  increases by a factor of 60 as  $E_{\tau_V}$  decreases by a factor of 100, while  $N(\text{HCO}^+)$  only increases by a factor of 3. Further reducing  $E_{\tau_V}$  increases both  $N(\text{CO})$  and  $N(\text{HCO}^+)$ . These effects are due to the large difference between the relaxation times of HCO $^+$  and CO that affect differently the total column densities, depending on the value of  $\tau_V$  (Eq. 5). The best range of vortex integral dissipations is  $10^{-13} \lesssim E_{\tau_V} \lesssim 10^{-12}$  erg cm $^{-1}$ , which corresponds to a vortex lifetime ranging between 100 yr and 1000 yr (for the standard vortex).

Interestingly, HCO $^+$  and CO depend differently on the other parameters. Both  $N(\text{CO})$  and  $N(\text{HCO}^+)$  decrease as  $a$  increases, HCO $^+$  is most sensitive to  $n_H$ , but is almost independent of  $A_V$ ,

while the reverse is true for CO. Adopting the best range for  $E_{\tau_V}$ , we find that the TDR model reproduces the observations for all the values  $10^{-11} \lesssim a \lesssim 10^{-10}$  s $^{-1}$ , in agreement with our previous work (Paper I). It is predicted that the detections of HCO $^+$  and CO trace a medium with a density comprised between 30 cm $^{-3}$  and 300 cm $^{-3}$  and a shielding  $A_V \gtrsim 0.2$  mag, i.e. a gas phase denser and more shielded from the UV photons than that inferred from the observations of CH $^+$  and SH $^+$ .

#### 7.4. Highly fragmented versus PDR-like medium

The predictions of the TDR model are now compared with the column densities of CO and H $_2$  observed in the SN, i.e. two species sensitive to the porosity of the gas to UV radiation (Fig. 7). The model parameters are set to their standard values. We adopt the two prescriptions for the extinction of the UV field discussed in Sect. 3.3: a homogeneous shielding along the line of sight (top panel) and a PDR-like shielding increasing with  $N_H$  (bottom panel). In both cases, we explore the impact of very small UV shielding (as small as 0.005 mag) on the column densities of CO predicted by the model.

The results shown in Fig. 7 confirm the results reported in the previous section and extend towards low column densities. They are in good agreement with the observations even for  $N(\text{H}_2)$  as

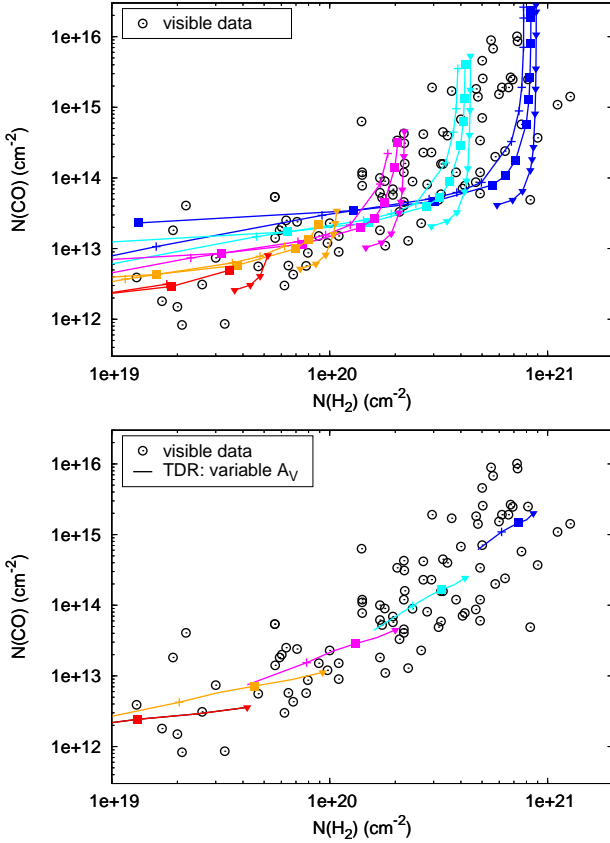


**Figure 7.** Observations of the column densities of CO and  $\text{H}_2$  (open circles, Sheffer et al. 2008) compared to the predictions of the TDR model. The model (filled symbols) are computed for several densities,  $n_{\text{H}} = 20$  (crosses), 50 (squares), and 300  $\text{cm}^{-3}$  (upside-down triangles) and total column densities,  $N_{\text{H}} = 1.1$  (red), 2.2 (orange), 4.5 (magenta), 9.0 (cyan), and 18 (blue)  $\times 10^{20} \text{ cm}^{-2}$ . *Top panel:* the lines of sight are reconstructed with a homogeneous shielding. The value adopted for  $A_V$  varies along each curve from left to right from 0.005 mag to  $A_{V,\text{max}}$ , where  $A_{V,\text{max}}$  is the shielding equivalent to a column density of matter of  $N_{\text{H}}/2$ . *Bottom panel:* the lines of sight are reconstructed with a PDR-like shielding function of  $N_{\text{H}}$  (Sect. 3.3), hence  $A_V$  is no longer a free parameter.

small as  $10^{19} \text{ cm}^{-2}$ . They also illustrate the influence of the fragmentation of the gas on  $N(\text{CO})$  and  $N(\text{H}_2)$ .

The predictions obtained with a highly fragmented medium (top panel) reproduce both the general increase in  $N(\text{CO})$  with  $N(\text{H}_2)$  and the large scatter of the data (about a factor of 10), whatever the other parameters. In this case, large column densities of CO at small  $N(\text{H}_2)$  are explained by the accumulation of many fragments, each weakly shielded from the UV field. We stress that  $A_V$  as low as 0.005 mag combined with large  $N_{\text{H}}$  might reproduce the largest CO column densities at low  $N(\text{H}_2)$ . A PDR-like reconstruction of the line of sight (bottom panel) reproduces the increase of  $N(\text{CO})$  on  $N(\text{H}_2)$  and especially the flattening at small  $N(\text{H}_2)$ . The  $N(\text{CO})/N(\text{H}_2)$  column density ratio is almost independent of the gas density. In this case, the observed scatter can only be explained by invoking variations of the other parameters over the acceptable ranges inferred in the previous sections.

Turbulent dissipation is therefore a crucial process to explain the CO abundances observed in the diffuse gas. The fragmentation of the gas and its permeability to UV photons has an important impact on the column densities of CO and molecular hydrogen. The two prescriptions discussed here (top and bottom panels of Fig. 7), however, are plausible scenarios, although the arguments developed in Sect. 2.3 on the broad width of the  $\text{H}/\text{H}_2$  transition region tend to favour a high level of fragmentation of the diffuse matter.

## 8. [CII] line emission versus far-infrared dust emission

### 8.1. Observational data

In this section we focus on the  $158 \mu\text{m}$  [CII] line observations performed by Ingalls et al. (2002) towards 101 translucent lines of sight at high Galactic latitudes. Their observational results are displayed in Fig. 8 as a function of the far-infrared dust brightness. They show that (1) the [CII] line and the interstellar dust emissions are linearly correlated  $I_{[\text{CII}]} = (2.5 \pm 0.9) \times 10^{-2} I_{\text{FIR}}$ , in agreement with the results of the COBE Galactic survey (Wright et al. 1991; Bennett et al. 1994); (2) this relation breaks for  $I_{\text{FIR}} \gtrsim 2.5 \times 10^{-4} \text{ erg cm}^{-2} \text{ s}^{-1} \text{ sr}^{-1}$  indicating a slower increase in [CII] emission at high values of far-infrared brightness (i.e. at high column densities of matter); and (3) the observed scatter is real.

Ingalls et al. (2002) interpreted these data in terms of a variable efficiency of the dust photoelectric heating in diffuse gas. Assuming that the cooling by [CII] entirely balances the heating by the UV photons, as expected in PDR environments, they deduced the heating rate in order to match the [CII] emission. Their best-fit scenario (thick black curve on the top panel of Fig. 8) is obtained for an efficiency of 4.3 % and a radiative energy flux of 1.6 times the standard value in the SN (Habing 1968). While plausible, this interpretation raises an issue: the best-fit value is larger than the 3 % obtained by Bakes & Tielens (1994) with the COBE Galactic survey and the range of efficiencies needed to reproduce the scatter exceeds the 5 % limit they prescribed.

### 8.2. Predictions of PDR models

The middle panel of Fig. 8 displays a comparison between the observations and the predictions of the Meudon PDR code computed for two densities  $n_{\text{H}} = 30$  and  $n_{\text{H}} = 100 \text{ cm}^{-3}$ , a radiation scaling factor  $\chi = 1$ , and a total amount of matter varying between 0.3 and 2 magnitudes. We adopt the conservative value of 3 % for the photoelectric heating efficiency. As found by Ingalls et al. (2002), a PDR-type medium naturally explains the slower increase in  $\text{C}^+$  emission at large  $I_{\text{FIR}}$  because at large visible extinction ( $A_V \gtrsim 1$  mag) the gas temperature is too low to excite the  $^2P_{3/2} \rightarrow ^2P_{1/2}$  transition of  $\text{C}^+$  and because  $\text{C}^+$  undergoes the  $\text{C}^+/\text{C}/\text{CO}$  transition. Once the transition is completed, the integrated emission of  $\text{C}^+$  across the slab tends towards a constant value regardless the total amount of matter along the line of sight. Yet, the comparison with the observations shows that PDR models computed with a photoelectric effect efficiency of 3 % underestimate by a factor 2 to 3 the observed  $\text{C}^+$  emission for  $I_{\text{FIR}} \gtrsim 2 \times 10^{-4} \text{ erg cm}^{-2} \text{ s}^{-1} \text{ sr}^{-1}$ .

### 8.3. Predictions of TDR models

To illustrate the impact of turbulent dissipation on the excitation of the [CII] line, we display in Fig. 9 the relative abundance of

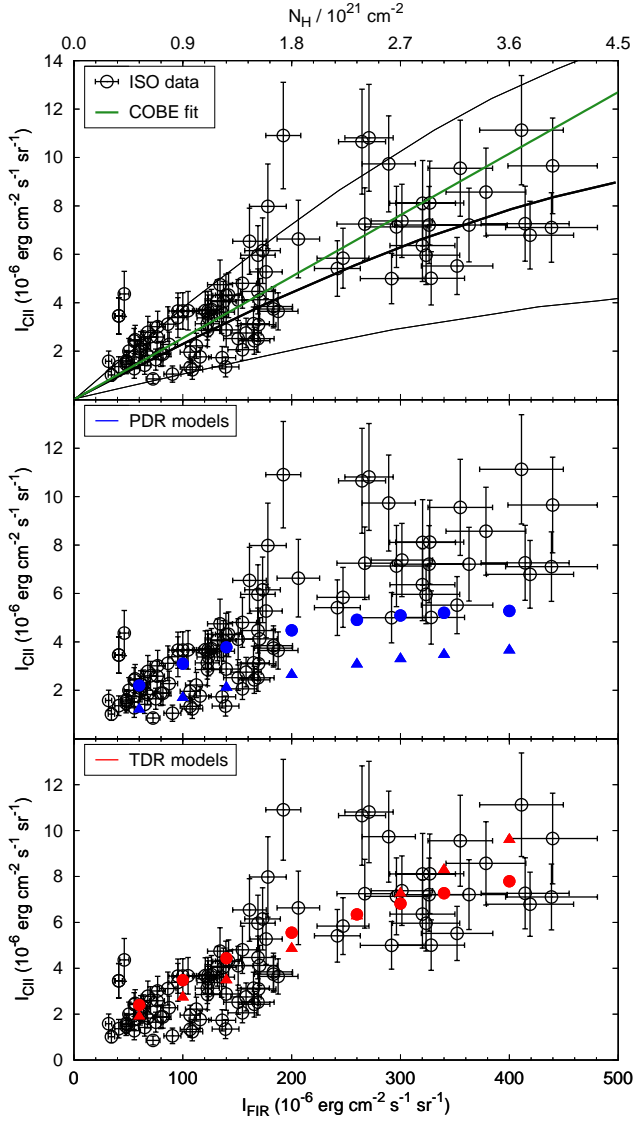


**Figure 8.** Intensities of the [CII] and of the far-infrared dust emission observed by Ingalls et al. (2002) at high Galactic latitudes (black empty circles) and comparison with the predictions of PDR (*middle panel*) and TDR (*bottom panel*) models. The black curves (*top panel*) are the PDR predictions of Ingalls et al. (2002) assuming a photoelectric heating efficiency of 7 %, 4.3 %, and 2 % from top to bottom. PDR and TDR models (blue and red filled symbols) are computed for  $a = 10^{-11} \text{ s}^{-1}$  and  $n_H = 30$  (triangles) and  $100 \text{ cm}^{-3}$  (circles), all other parameters are set to their standard values.

$\text{C}^+$  as a function of the position in an active vortex of the TDR model (top panel) and the cooling rate due to the [CII] line during the relaxation period (bottom panel) for a point located at the  $r_0$  radius of a vortex (see Sect. 3 and Paper I). We note that in this figure, the time axis is expressed in log units to allow the visualisation of the [CII] line cooling evolution. The origin at  $t = 10 \text{ yr}$  is somewhat arbitrary and is meant to allow a display of the [CII] emission close to the origin of the relaxation phase.

In an active vortex, the ignition of reaction 10 opens a fast chemical loop starting from  $\text{C}^+$  that successively increases the production of  $\text{CH}_2^+$ ,  $\text{CH}_3^+$ , and of neutral carbon (see Fig. C.1 of

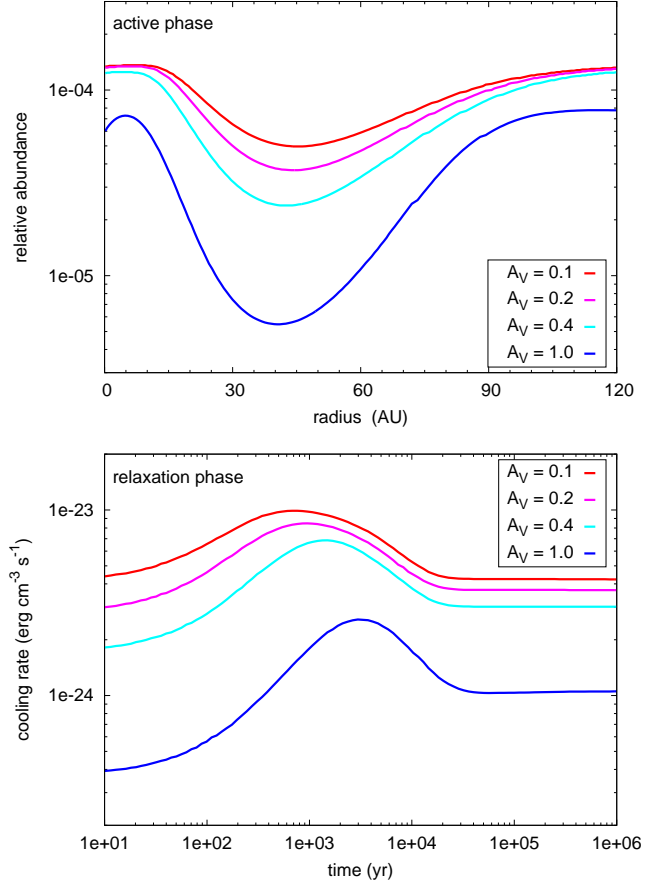


**Figure 9.** *Top panel:*  $\text{C}^+$  relative abundance as a function of the distance from the vortex axis during the active stage of the TDR model. *Bottom panel:* cooling rate associated with the  $^2P_{3/2} \rightarrow ^2P_{1/2}$  transition of  $\text{C}^+$  as a function of time during the relaxation stage of the TDR model. The model is computed for  $n_H = 100 \text{ cm}^{-3}$ ,  $a = 10^{-11} \text{ s}^{-1}$ , and several values of the visible extinction  $A_V$ : 0.1 (red), 0.2 (magenta), 0.4 (cyan), and 1.0 (blue) mag.

Appendix C). The bottleneck of this loop being the slow photoionisation of C, the abundance of  $\text{C}^+$  decreases across the active vortex (top panel of Fig. 9). The intensity of the [CII] line emitted during the active phase ( $I_{[\text{CII}]}$  at the shortest time (or before) in the bottom panel of Fig. 9), is therefore smaller than that emitted by the ambient medium ( $I_{[\text{CII}]}$  at times larger than a few  $10^4 \text{ yr}$  in the bottom panel of Fig. 9). Once the active stage stops, the abundance of  $\text{C}^+$  quickly increases up to its initial value, while the thermal relaxation lasts much longer. The outcome is a period during which the abundance of  $\text{C}^+$  is high and the temperature still high enough to enhance the [CII] emission. This period lasts for more than  $\sim 10^4 \text{ yr}$  while the active phase lasts only for a few hundred to one thousand years (see Sect. 7.3). Turbulent dissipation is therefore responsible for an enhancement of [CII] emission above that of the ambient gas.

The resulting [CII] intensities computed with TDR models combined with a PDR-like reconstruction of the line of sight are shown in the bottom panel of Fig. 8. For small values of the rate-of-strain, we find that the predictions of the model are in good agreement with the observations, that a PDR-like shielding function along the line of sight accounts for the slower increase in  $\text{C}^+$  emission at large  $I_{\text{FIR}}$  and that the scatter of observational data could be explained by two indistinguishable scenarios: either an



increase in the fragmentation of the gas or variations of  $\bar{\epsilon}$ ,  $E_{\tau_V}$ , or  $a$ .

The [CII] line emission of diffuse and translucent gas is therefore enhanced by the heating of the gas due to turbulent dissipation compared to PDR predictions.

## 9. Discussion

### 9.1. The turbulent dissipation scenario inferred from chemistry

The previous sections have shown that, despite unavoidable degeneracies, the comparison of the TDR model results with the observations identifies optimal ranges of three of the free parameters related to turbulent dissipation:  $\bar{\epsilon} \lesssim 10^{-23} \text{ erg cm}^{-3} \text{ s}^{-1}$  from the largest abundances of  $\text{CH}^+$ ,  $u_{\theta,M} \lesssim 3.5 \text{ km s}^{-1}$  from the  $\text{SH}^+/\text{CH}^+$  abundance ratio, and  $10^{-13} \lesssim E_{\tau_V} \lesssim 10^{-12} \text{ erg cm}^{-1}$  from the  $\text{CO}/\text{HCO}^+$  abundance ratio. We found in Paper I that the chemical properties of the diffuse ISM favour small rates-of-strain with the optimal range  $10^{-11} \lesssim a \lesssim 10^{-10} \text{ s}^{-1}$  that has been used in the present paper. Without fine tuning, these parameters reproduce the column densities of three additional molecular species OH,  $\text{H}_2\text{O}$ , and  $\text{C}_2\text{H}$ , and their link with those of  $\text{HCO}^+$ . They also reproduce the populations of the first five rotational levels of  $\text{H}_2$  observed in the local diffuse matter through UV absorption spectroscopy (Gry et al. 2002; Lacour et al. 2005) (Fig. 10). These results are in good agreement with those of Paper I, even though the chemical network has been updated (see Appendix A) because the local abundances of all these hydrides both in UV-driven and turbulence-driven chemistries are determined by only a handful of chemical reactions (see Appendix C), the rates of which are well constrained by laboratory experiments and theoretical calculations of reaction dynamics.

The outcome of the whole study is therefore an ensemble of four parameter ranges, related to turbulent dissipation, that have been determined independently from different molecular species, or pairs of species, and that satisfactorily reproduce the abundances of many other species observed in the diffuse ISM. We discuss in Sect. 9.3 how these values compare with the known properties of turbulence in the diffuse ISM.

### 9.2. Influence of the cosmic ray ionisation rate on the TDR model predictions

Since the low-energy cosmic ray fluxes cannot be observed from Earth (partly because of the interplanetary magnetic field) the current estimations of the cosmic ray ionisation rate of atomic or molecular hydrogen<sup>6</sup> ( $\zeta_{\text{H}}$  and  $\zeta_{\text{H}_2}$ , respectively) mostly rely on the observations of molecular tracers. Such methods are, however, uncertain because they strongly depend on the chemical models used to interpret the observations. Studies of dense clouds with OH,  $\text{HCO}^+$ , and HD indicate that  $\zeta_{\text{H}}$  is in the range  $1 - 5 \times 10^{-17} \text{ s}^{-1}$  with an average of  $\sim 3 \times 10^{-17} \text{ s}^{-1}$  (van der Tak & van Dishoeck 2000). Similarly, early studies of diffuse clouds with the same species have led to  $\zeta_{\text{H}} \sim 5 \times 10^{-17} \text{ s}^{-1}$  in the direction of  $\zeta$  Oph,  $\rho$  Per,  $\chi$  Oph,  $\zeta$  Per, and  $\xi$  Per (van Dishoeck & Black 1986; Federman et al. 1996b). However, the recent detections of  $\text{H}_3^+$  (McCall et al. 2004; Indriolo et al. 2007; Indriolo & McCall 2012),  $\text{OH}^+$ , and  $\text{H}_2\text{O}^+$  (Gerin et al. 2010a; Neufeld et al. 2010a; Indriolo et al. 2014) in the diffuse gas now point towards values considerably larger. Indeed the comparison of these data with chemical models solely driven

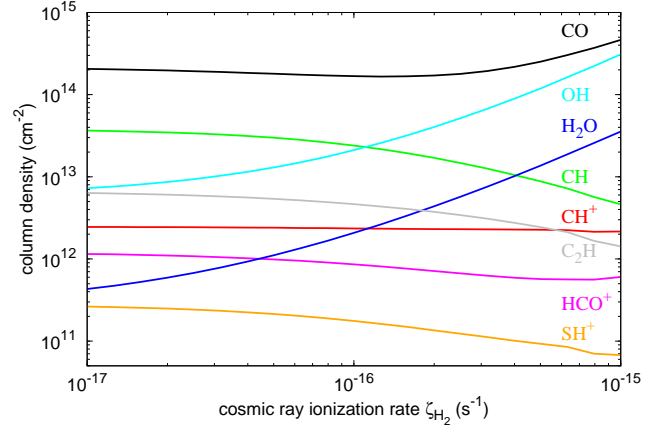


**Figure 11.** Column densities of CH,  $\text{CH}^+$ ,  $\text{SH}^+$ , OH,  $\text{H}_2\text{O}$ ,  $\text{HCO}^+$ , and CO predicted with the TDR model for a cloud of total column density  $N_{\text{H}} = 1.8 \times 10^{21} \text{ cm}^{-2}$  as functions of the  $\text{H}_2$  ionisation rate  $\zeta_{\text{H}_2}$ . All the other parameters of the code are set to their standard values (see main text).

by the UV radiation and the cosmic ray particles shows that  $\zeta_{\text{H}} \sim 2 \times 10^{-16} \text{ s}^{-1}$  on average (e.g. Hollenbach et al. 2012).

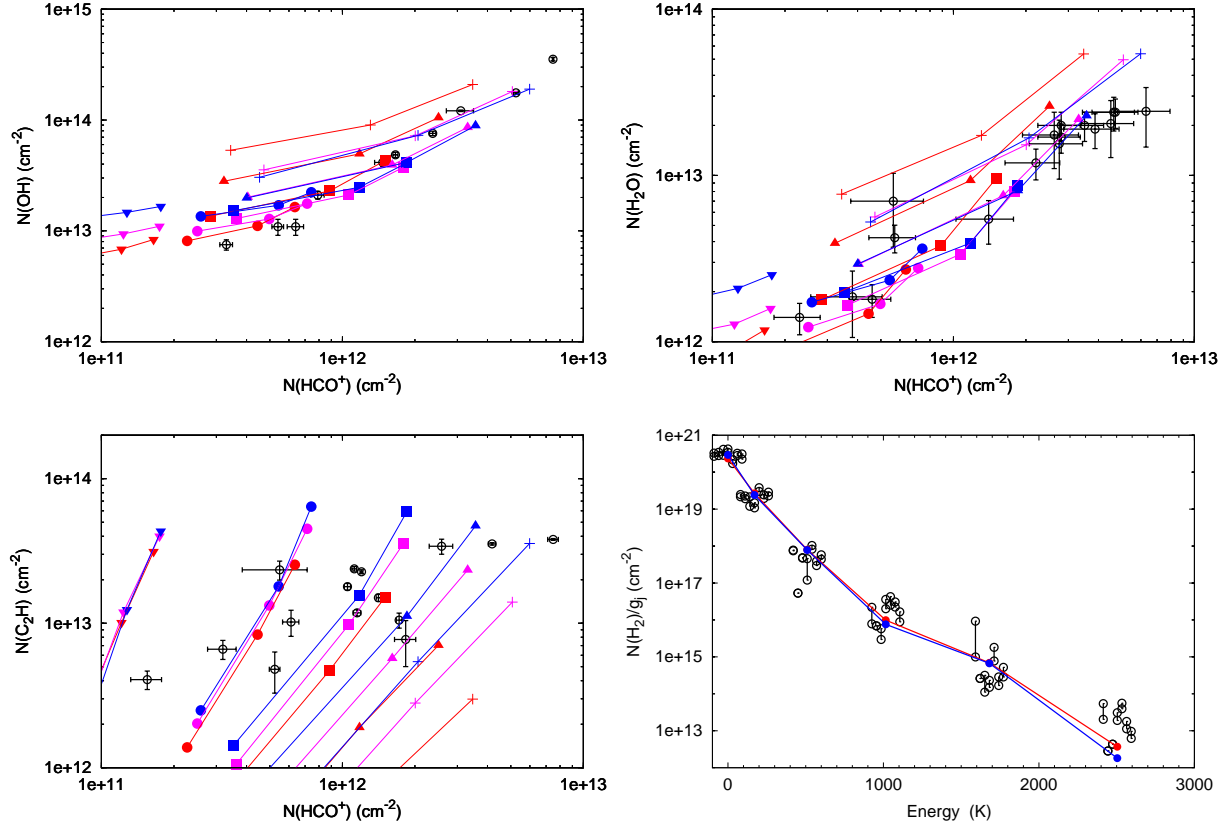
In this paper, we have therefore systematically run the TDR model for three different values of  $\zeta_{\text{H}_2}$ :  $3 \times 10^{-17}$ ,  $10^{-16}$ , and  $3 \times 10^{-16} \text{ s}^{-1}$ . In addition, and in order to further explore the impact of this parameter, 20 models were run covering the range  $10^{-17} \leq \zeta_{\text{H}_2} \leq 10^{-15} \text{ s}^{-1}$ ; all the other parameters were set to their standard values (see Sect. 4.1). The standard model,  $\zeta_{\text{H}_2} = 10^{-16} \text{ s}^{-1}$ , corresponds to the best-fit scenario of all the observational data (column densities and column density ratios) with the TDR model. We discuss here the sensitivity of our results to  $\zeta_{\text{H}_2}$ .

Figure 11 shows that most of the species considered in this work are not sensitive to the ionisation rate of  $\text{H}_2$ . The column densities of  $\text{CH}^+$ ,  $\text{SH}^+$ ,  $\text{HCO}^+$ , CO, and  $\text{C}_2\text{H}$  vary by less than a factor of four when  $\zeta_{\text{H}_2}$  increases by two orders of magnitude. It follows that  $\zeta_{\text{H}_2}$  has a limited impact on the determination of the properties of turbulent dissipation ( $\bar{\epsilon}$ ,  $u_{\theta,M}$ , and  $E_{\tau_V}$ , see Sects. 5, 6, and 7) and thus weakly affects the conclusions of this paper. In contrast, Fig. 11 shows that CH, OH, and  $\text{H}_2\text{O}$  are particularly sensitive to  $\zeta_{\text{H}_2}$ . The column density of CH decreases by a factor of 10 and those of OH and  $\text{H}_2\text{O}$  increase by two orders of magnitude when  $\zeta_{\text{H}_2}$  increases from  $10^{-17}$  to  $10^{-15} \text{ s}^{-1}$  because  $\zeta_{\text{H}_2}$  boosts both the productions of H and  $\text{H}^+$  which respectively destroy CH (via  $\text{CH} + \text{H} \rightarrow \text{C} + \text{H}_2$ ) and initiate the oxygen hydrogenation chain (via  $\text{O} + \text{H}^+ \rightarrow \text{O}^+ + \text{H}$ ).

In Fig. 10 we find that the column densities of OH and  $\text{H}_2\text{O}$  predicted with the TDR model are in good agreement with the observations for  $\zeta_{\text{H}_2} = 10^{-16} \text{ s}^{-1}$ . It is worth noting that the column density of CH predicted for this value ( $N(\text{CH}) \sim 2 \times 10^{13} \text{ cm}^{-2}$ ) is in agreement with those observed in the local diffuse medium along lines of sight with total column density  $N_{\text{H}} = 1.8 \times 10^{21} \text{ cm}^{-2}$  (Sheffer et al. 2008).

These results differ from those of Indriolo & McCall (2012), Hollenbach et al. (2012), and Indriolo et al. (2014) who found  $\zeta_{\text{H}_2} \sim 3 \times 10^{-16} \text{ s}^{-1}$  with PDR-type models and the recent observations of  $\text{H}_3^+$ ,  $\text{OH}^+$ , and  $\text{H}_2\text{O}^+$ . The main reason for this difference can be found in Fig. 3 which shows that the ambient medium accounts for only about 50 % of the column densities of OH and  $\text{H}_2\text{O}$  in the framework of the TDR model.

<sup>6</sup>  $\zeta_{\text{H}_2} = 2.3/1.7 \times \zeta_{\text{H}}$  (Glassgold & Langer 1974).



**Figure 10.** Observations compared to TDR model predictions. Data (open circles): column densities of HCO<sup>+</sup> and OH from Lucas & Liszt (1996) (*top left panel*), H<sub>2</sub>O from Flagey et al. (2013) (*top right panel*), C<sub>2</sub>H from Lucas & Liszt (2000) (*bottom left panel*), and the excited levels of H<sub>2</sub> from Gry et al. (2002) and Lacour et al. (2005) (*bottom right panel*). For clarity, in the bottom right panel the points for a given level are slightly shifted on the abscissa. Models (filled symbols): computed for  $A_V = 0.2$  (red), 0.4 (magenta), and 0.6 (blue) mag and  $n_H = 20$  (crosses), 30 (triangles), 50 (squares), and 300 (upside-down triangles)  $\text{cm}^{-3}$ . Except for the bottom right panel,  $\alpha$  increases along each curve from  $10^{-11}$  to  $10^{-10} \text{ s}^{-1}$  from right to left. In the bottom right panel, the models are shown for  $A_V = 0.1$  mag (red) and 0.4 mag (blue) and single values of the rate-of-strain  $a = 3 \times 10^{-11} \text{ s}^{-1}$  and the density  $n_H = 100 \text{ cm}^{-3}$ .

Indeed, it implies that the ionisation rate inferred from the TDR model is about two times smaller than that inferred from PDR-type models. In addition, as shown by Wolfire et al. (2008) and Hollenbach et al. (2012), the predictions of PDR-type models on carbon and oxygen chemistry depend on the details of the modeling of the polycyclic aromatic hydrocarbons (PAH) in the computation of the chemical reaction rates and in particular their size, geometry and abundances. The difference between our optimal value of  $\zeta_{\text{H}_2}$  and that deduced by Hollenbach et al. (2012) could therefore be due to the fact that we model PAHs as spherical particles of radius  $6.4 \text{ \AA}$  (or equivalently  $\sim 120$  carbon atoms) and relative abundance  $\sim 4 \times 10^{-7}$  while they consider planar PAHs containing 100 carbon atoms and with a relative abundance of  $2 \times 10^{-7}$ .

### 9.3. Consistency with known properties of turbulence in the diffuse ISM

The upper limit of  $\bar{\epsilon}$  was derived from the largest values of  $N(\text{CH}^+)/N_{\text{H}}$  detected in the diffuse medium towards the inner Galaxy. The parameter  $\bar{\epsilon}$  is the injection rate of turbulent energy at the large scales,  $\rho \sigma_l^3 / l$ , where  $\rho$  is the gas volumic mass and  $\sigma_l$  the rms velocity dispersion at scale  $l$ . This quantity is difficult to

determine observationally in the atomic gas because it involves a dynamical time  $l/\sigma_l$  and therefore a sizescale  $l$ , while the available data are only Gaussian velocity components. As discussed in Sect. 2, this value has been estimated in the atomic medium in only one region of the SN (Miville-Deschênes et al. 2003), so no statistics are available. In diffuse molecular gas traced by CO(1-0), large statistics are now available (Hennebelle & Falgarone 2012) and the upper limit on  $\bar{\epsilon}$  is of the order of the largest values of  $\bar{\epsilon}_{\text{obs}}$  measured at scales between 10 pc and 50 pc that can be considered as relevant large scales for turbulence in the diffuse medium. Moreover, these values are themselves averages measured at each of these large scales. The fact that CH<sup>+</sup> is not detected with average relative abundances larger than  $10^{-7}$  confirms previous estimations of the maximum turbulent energy density contained in the diffuse ISM. The lower limit of  $N(\text{CH}^+)/N_{\text{H}}$  cannot be exploited because it comes from the sensitivity limit of the observations. The observed large scatter by a factor of  $\sim 10$  of the CH<sup>+</sup> abundance (Fig. 4) could be interpreted by the fact that the formation of CH<sup>+</sup> is highly intermittent: the CH<sup>+</sup> abundance traces subsets of the CNM where the turbulent transfer rate is above average, hence driving an above-average dissipation rate. The above-average dissipation

rate needs nonetheless to heat the gas to temperatures that compare with the endothermicity threshold of the  $\text{CH}^+$  formation.

The upper limit on the ion-neutral drift velocity rules out values larger than  $3.5 \text{ km s}^{-1}$ . In the model, this velocity drift is set by the maximum tangential velocity of the vortex, which is itself linked to the velocity dispersion of the ambient turbulence, i.e. a property of turbulence discussed in Sect. 3. It is noteworthy that this value of  $3.5 \text{ km s}^{-1}$  is close to the large-scale velocity dispersion of the CNM seen in the HI line (Miville-Deschênes et al. 2003; Haud & Kalberla 2007) and is also representative of the internal velocity dispersion of the diffuse molecular gas at scales of  $10 - 50 \text{ pc}$ . The parameters relevant to the ambient turbulence, inferred independently from the  $\text{CH}^+$  and  $\text{SH}^+$  abundances, are therefore broadly consistent with our knowledge of turbulence in the diffuse medium.

#### 9.4. Internal coherence

We now turn to the parameters controlling the dynamics of the dissipative regions and compare the different associated timescales. The optimal range of rates-of-strain given above corresponds to timescales  $a^{-1}$  varying between 300 yr and 3000 yr. The independent determination of the burst lifetime,  $\tau_v$ , is in the range  $100 - 1000 \text{ yr}$  for the reference vortex (see Sect. 7). Finally, the turnover timescale of a vortex,  $2\pi r_0/u_{\theta,M}$  is of the order of  $10^3 \text{ yr}$  for  $r_0 = 100 \text{ au}$  and  $u_{\theta,M} = 3 \text{ km s}^{-1}$ . All these timescales are therefore commensurate, confirming the picture of a highly non-equilibrium chemistry driven by turbulent dissipation bursts over timescales as short as 100 yr and size scales of  $\sim 100 \text{ au}$ . It is interesting to note that the small values of  $a$ , favoured by the chemistry, lead to timescales longer than the vortex lifetime, i.e. the action of the rate-of-strain lasts at least as long as the vortex lifetime.

#### 9.5. Limitations of the TDR model

Some of the limitations of the TDR model have already been discussed in Paper I. In particular, the use of only one type of dissipation burst was mentioned, while dissipation is known to be distributed among a large number of bursts of different strengths (Mouri & Hori 2009). The warm chemistry being driven by endoenergetic reactions with exponential thresholds, the abundances and abundance ratios of several species greatly depend on the strength of the burst as long as the corresponding thresholds are not overcome (see Sect. 6). A distribution of bursts could thus have an important impact. Implementing such a distribution in the TDR code would require defining additional parameters that cannot be constrained with the current observations of the diffuse ISM.

Our model is idealised, but the results rely on two robust properties of gas-phase interstellar chemistry: the large differences of endothermicities and the orders of magnitude differences between relaxation times due to the various destruction mechanisms (photodissociation, recombination, collisions with H and  $\text{H}_2$ ). Hence, the results of the TDR model presented here do not depend on the details of the treatment of the regions of dissipation. Its originality relies in the exploitation of the fact that the chemical timescales in the diffuse medium are commensurate with the smallest dynamical times of turbulence, at which its huge reservoir of energy is dissipated.

#### 9.6. Turbulent dissipation in vortices and shear layers or C-shocks?

The problem raised by the high abundances of  $\text{CH}^+$  in the diffuse medium was recognised several decades ago. Additional gas heating mechanisms were invoked and modelled to reproduce the observed column densities: gas heating behind shocks associated with HII regions expansion (Elitzur & Watson 1978), ion-neutral friction in shocks with magnetic precursors, i.e. C-shocks (Draine & Katz 1986; Pineau des Forêts et al. 1986), or in Alfvén waves that also involve the streaming of  $\text{C}^+$  relative to  $\text{H}_2$  (Federman et al. 1996a).

To favour one scenario over the others from the sole observations of chemical abundances and line profiles is difficult. For instance  $\text{CH}^+$  could be explained by one C-shock with a velocity of  $10\text{--}12 \text{ km s}^{-1}$  leading to a predicted velocity shift between  $\text{CH}^+$  and CH of  $2 \text{ km s}^{-1}$  at most, i.e. if the shock propagates along the line of sight (Flower & Pineau des Forêts 1998). Yet, it is more likely that several low velocity shock waves will be present along the line of sight, with different orientations and velocities. Gredel et al. (2002) proposed such a model with  $\sim 20$  C-shocks of velocities of  $\sim 8 \text{ km s}^{-1}$  per  $A_V$ , leading to a velocity shift between CH and  $\text{CH}^+$  smaller than  $1 \text{ km s}^{-1}$ .

However, it is now understood that shocks are not the only structures where dissipation is concentrated in compressible turbulence. In transonic hydrodynamic turbulence, Porter et al. (2002) found that the interaction of shocks generates vorticity, resulting in only a small fraction of the kinetic energy left in compressional modes. In supersonic MHD turbulence, the dynamic alignment of velocity and magnetic fields tends to Alfvénize turbulence, a process at the origin of the low ratio of the energy density in compressional to solenoidal modes (Kritsuk et al. 2010). Similar conclusions were found in other simulations of MHD turbulence where incompressible modes carry more than 70 % of the total kinetic energy (Vestuto et al. 2003). It is for these reasons that we chose to investigate the chemical signatures of turbulent dissipation in vortices.

### 10. Conclusions

The vast diversity of the chemical formation and destruction pathways of atoms and molecules, and of their timescales in particular, provide unique clues to the non-equilibrium physical processes driving the thermal and chemical evolution of the diffuse ISM that have never been investigated before. In this paper we have presented a comprehensive study of the chemical composition of diffuse matter in the framework of UV-driven and turbulence-driven chemistries. The analysis focuses on 16 different atomic and molecular species observed towards several hundred sightlines sampling the SN and the inner Galaxy diffuse medium.

We have distinguished the species that are the most sensitive to turbulent dissipation (the abundances of  $\text{CH}^+$  and  $\text{SH}^+$ , and the populations of the  $J = 3, 4, 5$  rotational levels of  $\text{H}_2$ ) from those that are not and trace the interaction between the UV radiation field and the interstellar matter (H,  $\text{H}_2$ , HF, and the  $J = 0, 1, 2$  excited levels of  $\text{H}_2$ ). The column densities of CO and  $\text{HCO}^+$  and the intensity of the [CII] line emission are also found to be sensitive to turbulent dissipation.

The chemical differences among all these species are so pronounced that robust results on the turbulent cascade in the diffuse ISM can be inferred from the observations of specific pairs of species. In the framework of the TDR model, we find that (1) the  $\text{CH}^+$  abundance is proportional to the average turbulent dissipa-

tion rate, thus to the average energy transfer rate in the turbulent cascade; (2) the  $\text{SH}^+/\text{CH}^+$  abundance ratio sets an upper limit to the ion-neutral velocity drift in the active dissipation regions because of the large difference of endothermicities involved in the formation of these two species; and (3) the  $\text{HCO}^+/\text{CO}$  abundance ratio sets the lifetime of the active dissipation bursts because of the large difference of destruction timescales of these two species. We find that the increase in  $\text{CH}^+$  abundance in the inner Galaxy compared to the value derived in the local ISM could be due to an increase in the turbulent injection rate towards the inner Galaxy. This set of independently determined properties provides a coherent scenario in which the regions of active dissipation of turbulence in the diffuse ISM are small-scale (a few 100 au) short-lived ( $\sim 100 - 1000$  yr) bursts in which dissipation is mainly due to ion-neutral decoupling ( $\sim 3 \text{ km s}^{-1}$ ) rather than viscous friction. These results are in good agreement with independent determinations of the turbulence properties in the diffuse ISM and with the fundamental properties of turbulence known from laboratory experiments.

We also show for the first time that turbulent dissipation plays a crucial role in the formation of diffuse interstellar CO and stress the influence of the fragmentation of the gas on the observed correlation between CO and molecular hydrogen: large column densities of CO at low  $N(\text{H}_2)$  may result from the accumulation on the line of sight of fragments, each weakly shielded from the UV radiation field. Finally, we show that turbulent dissipation enhances the  $[\text{CII}]$  line emission in translucent environments by a factor of  $\sim 2$  compared to the value obtained if the gas heating was solely driven by UV photons.

These results shed a new light on the interpretation of atomic and molecular data and provide templates for the analysis of future observations of diffuse environments in Galactic and extragalactic sources.

**Acknowledgements.** We are most grateful to James G. Ingalls for providing the data used in Fig. 8.

## References

- Agúndez, M., Goicoechea, J. R., Cernicharo, J., Faure, A., & Roueff, E. 2010, *ApJ*, 713, 662
- Anders, E. & Grevesse, N. 1989, *Geochim. Cosmochim. Acta*, 53, 197
- Anicich, V. G. 2003, JPL Publication
- Arnéodo, A., Benzi, R., Berg, J., et al. 2008, *Physical Review Letters*, 100, 4504
- Bakes, E. L. O. & Tielens, A. G. G. M. 1994, *ApJ*, 427, 822
- Bakes, E. L. O. & Tielens, A. G. G. M. 1998, *ApJ*, 499, 258
- Bennett, C. L., Fixsen, D. J., Hinshaw, G., et al. 1994, *ApJ*, 434, 587
- Bron, E., Le Bourlot, J., & Le Petit, F. 2014, *A&A*, in press.
- Burgh, E. B., France, K., & McCandliss, S. R. 2007, *ApJ*, 658, 446
- Casavecchia, P. 2000, *Reports on Progress in Physics*, 63, 355
- Compiègne, M., Verstraete, L., Jones, A., et al. 2011, *A&A*, 525, A103
- Cox, D. P. 2005, *ARA&A*, 43, 337
- Crane, P., Lambert, D. L., & Sheffer, Y. 1995, *ApJS*, 99, 107
- Daflon, S. & Cunha, K. 2004, *ApJ*, 617, 1115
- Dalgarno, A. 2006, *Proceedings of the National Academy of Science*, 103, 12269
- De Luca, M., Gupta, H., Neufeld, D., et al. 2012, *ApJ*, 751, L37
- Douady, S., Couder, Y., & Brachet, M. E. 1991, *Physical Review Letters*, 67, 983
- Draine, B. T. & Bertoldi, F. 1996, *ApJ*, 468, 269
- Draine, B. T. & Katz, N. 1986, *ApJ*, 310, 392
- Draine, B. T. & Li, A. 2007, *ApJ*, 657, 810
- Draine, B. T. & Sutin, B. 1987, *ApJ*, 320, 803
- Elitzur, M. & Watson, W. D. 1978, *A&A*, 70, 443
- Falgarone, E., Godard, B., Cernicharo, J., et al. 2010a, *A&A*, 521, L15
- Falgarone, E., Ossenkopf, V., Gerin, M., et al. 2010b, *A&A*, 518, L118
- Falgarone, E., Pety, J., & Hily-Blant, P. 2009, *A&A*, 507, 355
- Falgarone, E., Verstraete, L., Pineau Des Forêts, G., & Hily-Blant, P. 2005, *A&A*, 433, 997
- Federman, S. R., Glassgold, A. E., & Kwan, J. 1979, *ApJ*, 227, 466
- Federman, S. R., Rawlings, J. M. C., Taylor, S. D., & Williams, D. A. 1996a, *MNRAS*, 279, L41
- Federman, S. R., Weber, J., & Lambert, D. L. 1996b, *ApJ*, 463, 181
- Fich, M. & Tremaine, S. 1991, *ARA&A*, 29, 409
- Fitzpatrick, E. L. & Spitzer, Jr., L. 1997, *ApJ*, 475, 623
- Flagey, N., Goldsmith, P. F., Lis, D. C., et al. 2013, *ApJ*, 762, 11
- Florescu-Mitchell, A. I. & Mitchell, J. B. A. 2006, *Phys. Rep.*, 430, 277
- Flower, D. R. & Pineau des Forêts, G. 1998, *MNRAS*, 297, 1182
- Flower, D. R., Pineau des Forêts, G., & Hartquist, T. W. 1985, *MNRAS*, 216, 775
- Flower, D. R. & Roueff, E. 1998a, *Journal of Physics B Atomic Molecular Physics*, 31, L955
- Flower, D. R. & Roueff, E. 1998b, *Journal of Physics B Atomic Molecular Physics*, 31, 2935
- Flower, D. R., Roueff, E., & Zeippen, C. J. 1998, *Journal of Physics B Atomic Molecular Physics*, 31, 1105
- Gerin, M., de Luca, M., Black, J., et al. 2010a, *A&A*, 518, L110
- Gerin, M., de Luca, M., Goicoechea, J. R., et al. 2010b, *A&A*, 521, L16
- Gerin, M., Ruaud, M., Goicoechea, J. R., et al. 2014, *A&A*, accepted
- Gerlich, D., Disch, R., & Scherbarth, S. 1987, *J. Chem. Phys.*, 87, 350
- Gillmon, K., Shull, J. M., Tumlinson, J., & Danforth, C. 2006, *ApJ*, 636, 891
- Glassgold, A. E. & Langer, W. D. 1974, *ApJ*, 193, 73
- Godard, B., Falgarone, E., Gerin, M., Hily-Blant, P., & de Luca, M. 2010, *A&A*, 520, A20+
- Godard, B., Falgarone, E., Gerin, M., et al. 2012, *A&A*, 540, A87
- Godard, B., Falgarone, E., & Pineau des Forêts, G. 2009, *A&A*, 495, 847
- Goldsmith, P. F. 2013, *ApJ*, 774, 134
- Gredel, R. 1997, *A&A*, 320, 929
- Gredel, R., Pineau des Forêts, G., & Federman, S. R. 2002, *A&A*, 389, 993
- Gry, C., Boulanger, F., Nehmé, C., et al. 2002, *A&A*, 391, 675
- Habing, H. J. 1968, *Bull. Astron. Inst. Netherlands*, 19, 421
- Hassel, G. E., Herbst, E., & Bergin, E. A. 2010, *A&A*, 515, A66
- Haud, U. & Kalberla, P. M. W. 2007, *A&A*, 466, 555
- Heiles, C. & Troland, T. H. 2003, *ApJ*, 586, 1067
- Hennebelle, P. & Falgarone, E. 2012, *A&A Rev.*, 20, 55
- Herbst, E. 1985, *ApJ*, 291, 226
- Hierl, P. M., Morris, R. A., & Viggiano, A. A. 1997, *J. Chem. Phys.*, 106, 10145
- Hollenbach, D., Kaufman, M. J., Neufeld, D., Wolfire, M., & Goicoechea, J. R. 2012, *ApJ*, 754, 105
- Indriolo, N., Geballe, T. R., Oka, T., & McCall, B. J. 2007, *ApJ*, 671, 1736
- Indriolo, N. & McCall, B. J. 2012, *ApJ*, 745, 91
- Indriolo, N., Neufeld, D. A., Gerin, M., et al. 2014, *ApJ*, submitted
- Ingalls, J. G., Bania, T. M., Boulanger, F., et al. 2011, *ApJ*, 743, 174
- Ingalls, J. G., Reach, W. T., & Bania, T. M. 2002, *ApJ*, 579, 289
- Jenkins, E. B. & Tripp, T. M. 2011, *ApJ*, 734, 65
- Jimenez, J. 1997, *Euromech Colloquium*, 384
- Joulain, K., Falgarone, E., Pineau des Forêts, G., & Flower, D. 1998, *A&A*, 340, 241
- Kalberla, P. M. W. & Kerp, J. 2009, *ARA&A*, 47, 27
- Kim, C.-G., Ostriker, E. C., & Kim, W.-T. 2013, *ApJ*, 776, 1
- Kritsuk, A. G., Norman, M. L., Padoan, P., & Wagner, R. 2007, *ApJ*, 665, 416
- Kritsuk, A. G., Ustyugov, S. D., Norman, M. L., & Padoan, P. 2010, in *Astronomical Society of the Pacific Conference Series*, Vol. 429, *Numerical Modeling of Space Plasma Flows*, Astronom-2009, ed. N. V. Pogorelov, E. Audit, & G. P. Zank, 15
- Lacour, S., Ziskin, V., Hébrard, G., et al. 2005, *ApJ*, 627, 251
- Laor, A. & Draine, B. T. 1993, *ApJ*, 402, 441
- Le Bourlot, J., Le Petit, F., Pinto, C., Roueff, E., & Roy, F. 2012, *A&A*, 541, A76
- Le Bourlot, J., Pineau des Forêts, G., & Flower, D. R. 1999, *MNRAS*, 305, 802
- Le Petit, F., Nehmé, C., Le Bourlot, J., & Roueff, E. 2006, *ApJS*, 164, 506
- Lee, H.-H., Herbst, E., Pineau des Forêts, G., Roueff, E., & Le Bourlot, J. 1996, *A&A*, 311, 690
- Lepp, S., Dalgarno, A., van Dishoeck, E. F., & Black, J. H. 1988, *ApJ*, 329, 418
- Levine, R. D. 2005, *Molecular Reaction Dynamics*
- Levrier, F., Le Petit, F., Hennebelle, P., et al. 2012, *A&A*, 544, A22
- Liszt, H. & Lucas, R. 2001, *A&A*, 370, 576
- Liszt, H. & Lucas, R. 2004, *A&A*, 428, 445
- Liszt, H. S. & Lucas, R. 1998, *A&A*, 339, 561
- Liszt, H. S. & Pety, J. 2012, *A&A*, 541, A58
- Liszt, H. S., Pety, J., & Lucas, R. 2010, *A&A*, 518, A45
- Lucas, R. & Liszt, H. 1996, *A&A*, 307, 237
- Lucas, R. & Liszt, H. S. 2000, *A&A*, 358, 1069
- Lumsden, S. L., Hoare, M. G., Urquhart, J. S., et al. 2013, *ApJS*, 208, 11
- Magnani, L. & Salzer, J. J. 1989, *AJ*, 98, 926
- Magnani, L. & Salzer, J. J. 1991, *AJ*, 101, 1429
- Mathis, J. S., Mezger, P. G., & Panagia, N. 1983, *A&A*, 128, 212
- McCall, B. J., Huneycutt, A. J., Saykally, R. J., et al. 2004, *Phys. Rev. A*, 70, 052716

McElroy, D., Walsh, C., Markwick, A. J., et al. 2013, *A&A*, 550, A36

McEwan, M. J., Scott, G. B. I., Adams, N. G., et al. 1999, *ApJ*, 513, 287

Menten, K. M., Wyrowski, F., Belloche, A., et al. 2011, *A&A*, 525, A77+

Millar, T. J. & Hobbs, L. M. 1988, *MNRAS*, 231, 953

Mininni, P. D., Alexakis, A., & Pouquet, A. 2006a, *Phys. Rev. E*, 74, 016303

Mininni, P. D., Pouquet, A. G., & Montgomery, D. C. 2006b, *Physical Review Letters*, 97, 244503

Miville-Deschênes, M.-A., Joncas, G., Falgarone, E., & Boulanger, F. 2003, *A&A*, 411, 109

Moisy, F. & Jiménez, J. 2004, *Journal of Fluid Mechanics*, 513, 111

Momferratos, G., Lesaffre, P., Falgarone, E., & Pineau des Forêts, G. 2014, *MNRAS*, in press.

Monje, R. R., Lis, D. C., Roueff, E., et al. 2013, *ApJ*, 767, 81

Moskalenko, I. V., Porter, T. A., & Strong, A. W. 2006, *ApJ*, 640, L155

Mouri, H. & Hori, A. 2009, *Fluid Dynamics Research*, 41, 021402

Mouri, H., Hori, A., & Kawashima, Y. 2007, *Physics of Fluids*, 19, 055101

Nagaoka, K., Okamoto, A., Yoshimura, S., Kono, M., & Tanaka, M. Y. 2002, *Physical Review Letters*, 89, 075001

Nagy, Z., Van der Tak, F. F. S., Ossenkopf, V., et al. 2013, *A&A*, 550, A96

Neufeld, D. A., Falgarone, E., Gerin, M., et al. 2012, *A&A*, 542, L6

Neufeld, D. A., Goicoechea, J. R., Sonnentrucker, P., et al. 2010a, *A&A*, 521, L10

Neufeld, D. A., Sonnentrucker, P., Phillips, T. G., et al. 2010b, *A&A*, 518, L108

Neufeld, D. A. & Wolfire, M. G. 2009, *ApJ*, 706, 1594

Nolan, D. S. & Farrell, B. F. 1999, *Journal of Atmospheric Sciences*, 56, 2908

Padovani, M. & Galli, D. 2013, in *Advances in Solid State Physics*, Vol. 34, *Cosmic Rays in Star-Forming Environments*, ed. D. F. Torres & O. Reimer, 61

Pineau des Forêts, G., Roueff, E., & Flower, D. R. 1986, *MNRAS*, 223, 743

Porter, D., Pouquet, A., & Woodward, P. 2002, *Phys. Rev. E*, 66, 026301

Porter, T. A. & Strong, A. W. 2005, in *International Cosmic Ray Conference*, Vol. 4, *International Cosmic Ray Conference*, 77

Rachford, B. L., Snow, T. P., Tumlinson, J., et al. 2002, *ApJ*, 577, 221

Rangwala, N., Maloney, P. R., Glenn, J., et al. 2011, *ApJ*, 743, 94

Savage, B. D. & Sembach, K. R. 1996, *ARA&A*, 34, 279

Sheffer, Y., Rogers, M., Federman, S. R., et al. 2008, *ApJ*, 687, 1075

Snow, T. P., Destree, J. D., & Jensen, A. G. 2007, *ApJ*, 655, 285

Snow, T. P. & McCall, B. J. 2006, *ARA&A*, 44, 367

Sofia, U. J. & Meyer, D. M. 2001, *ApJ*, 554, L221

Sonnentrucker, P., Neufeld, D. A., Phillips, T. G., et al. 2010, *A&A*, 521, L12+

Sultanov, R. A. & Balakrishnan, N. 2005, *ApJ*, 629, 305

Tanahashi, M., Kang, S.-J., Miyamoto, T., Shiohara, S., & T., M. 2004, *Int. J. Heat Fluid Flow*, 25, 331

Uritsky, V. M., Pouquet, A., Rosenberg, D., Mininni, P. D., & Donovan, E. F. 2010, *Phys. Rev. E*, 82, 056326

Urquhart, J. S., Figura, C. C., Moore, T. J. T., et al. 2014, *MNRAS*, 437, 1791

van der Tak, F. F. S. & van Dishoeck, E. F. 2000, *A&A*, 358, L79

van der Werf, P. P., Isaak, K. G., Meijerink, R., et al. 2010, *A&A*, 518, L42

van Dishoeck, E. F. 1988, in *Rate Coefficients in Astrochemistry*. Editors, T. J. Millar, D. A. Williams; Publisher, Kluwer Academic Publishers., ed. T. J. Millar & D. A. Williams, 49

van Dishoeck, E. F. & Black, J. H. 1986, *ApJS*, 62, 109

van Dishoeck, E. F. & Black, J. H. 1988, *ApJ*, 334, 771

van Dishoeck, E. F., Jonkheid, B., & van Hemert, M. C. 2006, *Faraday Discussions*, 133, 231

Vestuto, J. G., Ostriker, E. C., & Stone, J. M. 2003, *ApJ*, 590, 858

Visser, R., van Dishoeck, E. F., & Black, J. H. 2009, *A&A*, 503, 323

Wainscoat, R. J., Cohen, M., Volk, K., Walker, H. J., & Schwartz, D. E. 1992, *ApJS*, 83, 111

Wakelam, V., Herbst, E., Loison, J.-C., et al. 2012, *ApJS*, 199, 21

Weingartner, J. C. & Draine, B. T. 2001a, *ApJ*, 563, 842

Weingartner, J. C. & Draine, B. T. 2001b, *ApJS*, 134, 263

Welty, D. E., Hobbs, L. M., & Morton, D. C. 2003, *ApJS*, 147, 61

Weselak, T., Galazutdinov, G. A., Musaev, F. A., & Krelowski, J. 2008, *A&A*, 484, 381

Wolfire, M. G., Tielens, A. G. G. M., Hollenbach, D., & Kaufman, M. J. 2008, *ApJ*, 680, 384

Woodall, J., Agúndez, M., Markwick-Kemper, A. J., & Millar, T. J. 2007, *A&A*, 466, 1197

Wright, E. L., Mather, J. C., Bennett, C. L., et al. 1991, *ApJ*, 381, 200

Zanchet, A., Godard, B., Bulut, N., et al. 2013, *ApJ*, 766, 80

Zellner, R. & Steinert, W. 1981, *Chemical Physics Letters*, 81, 568

**Table A.1.** Elemental abundances  $[X] = n(X)/n_H$  used in the TDR model as measured in the local interstellar medium (Anders & Grevesse 1989; Savage & Sembach 1996; Sofia & Meyer 2001; Snow et al. 2007).

[He]	$1.00 \times 10^{-01}$
[C]	$1.38 \times 10^{-04}$
[O]	$3.02 \times 10^{-04}$
[N]	$7.94 \times 10^{-05}$
[S]	$1.86 \times 10^{-05}$
[F]	$1.80 \times 10^{-08}$
[Cl]	$1.00 \times 10^{-07}$
[Fe]	$1.50 \times 10^{-08}$

## Appendix A: Treatment of the chemistry

In our previous papers (Godard et al. 2009, 2010, 2012), the chemical network implemented in the TDR model was built as a combination of the chemical network of the Meudon PDR code (Le Petit et al. 2006) and those extracted from the main on-line databases for astrochemistry<sup>7</sup>, UMIST (Woodall et al. 2007; McElroy et al. 2013), OSU (Hassel et al. 2010), and KIDA (Wakelam et al. 2012). To improve the usefulness of the model we break here from the previous approach and choose to adopt the chemical network of the Meudon PDR code (available at <http://pdr.obspm.fr/PDRcode.html>) except for a few special cases presented below.

### A.1. Chlorine and fluorine chemistries

By default the chemical network of the Meudon PDR code contains 133 gas-phase atomic and molecular compounds – including hydrogen-, helium-, carbon-, nitrogen-, oxygen-, sulfur-, silicon-, and iron-bearing species – which interact with one another through 2631 gas-phase reactions. In order to obtain TDR predictions concerning the abundances of HF, HCl, and HCl<sup>+</sup>, all recently detected in the diffuse ISM with Herschel/HIFI (Neufeld et al. 2010b; Sonnentrucker et al. 2010; Monje et al. 2013; De Luca et al. 2012), the network has been expanded to 14 chlorine- and fluorine-bearing species: Cl, HCl, CCl, Cl<sup>+</sup>, HCl<sup>+</sup>, H<sub>2</sub>Cl<sup>+</sup>, CCl<sup>+</sup>, H<sub>2</sub>CCl<sup>+</sup>, F, HF, F<sup>+</sup>, HF<sup>+</sup>, H<sub>2</sub>F<sup>+</sup>, and CF<sup>+</sup>. This additional network includes the 38 chemical reactions given in the recent review of experimental and theoretical studies performed by Neufeld & Wolfire (2009). Their rates are those of Neufeld & Wolfire (2009) except for the photodissociation of HF, HCl, and HCl<sup>+</sup> and the photoionisation of Cl, the rates of which are taken from the UMIST database (McElroy et al. 2013) and the calculations of van Dishoeck (1988) and van Dishoeck et al. (2006). This additional network also includes the 38 ion-neutral and dissociative recombination reactions given by Anicich (2003) and the OSU database for astrochemistry (Hassel et al. 2010).

### A.2. Photoreactions

Since the amounts of matter of prototypical diffuse and translucent environments (Snow & McCall 2006) are insufficient to entirely absorb the mean interstellar UV radiation field, both photoionisation and photodissociation are known to play a major

<sup>7</sup> available at <http://www.udfa.net/>, <http://kida.obs.u-bordeaux1.fr>, and <http://www.physics.ohio-state.edu/~eric/research.html>.



role in the destruction of atoms and molecules in the diffuse ISM. In the Meudon PDR code (Le Petit et al. 2006) both processes are treated self-consistently by solving the UV radiative transfer as a function of position in a plan parallel slab – including the absorption by molecular lines and the absorption and scattering by interstellar dust – and by computing at each point the photodestruction rates from the integration of the cross sections over the specific intensity of the UV radiation.

Such a detailed approach cannot, however, be applied to the TDR code since the radiative transfer is modelled with a single parameter, the extinction at visible wavelength  $A_V$ , assumed to be constant over the entire sightline (standard case, see Sect 3.3). The photo-reaction rates are thus computed as

$$k_\gamma = \gamma \exp(-\beta A_V) \text{ s}^{-1}, \quad (\text{A.1})$$

where  $\gamma$  and  $\beta$  are constants taken from van Dishoeck (1988) and van Dishoeck et al. (2006) who performed fits of the photodestruction rates over the range  $A_V = 0 - 3$  mag, assuming a slab of gas with constant density illuminated on one side and where the extinction is only the result of the absorption and scattering by  $0.1 \mu\text{m}$  large interstellar grains.

While this expression is reliable for the photodissociation occurring though continuous absorption, it is however too simplistic to correctly describe the photodissociation by line absorption processes which strongly depends on the self-shielding, i.e. the column density of the molecule from the edge of the cloud up to  $A_V$ . We therefore apply Eq. A.1 to all molecules except for  $\text{H}_2$  and CO whose photodissociation is known to occur through line processes (Lee et al. 1996; Draine & Bertoldi 1996; Visser et al. 2009). For these two species we adopt the photo-reaction rates computed with the Meudon PDR code assuming a slab of gas with constant density illuminated on one side. The details of these results and their implementation in the TDR model are described in Appendix B.

### A.3. Excitation of $\text{H}_2$

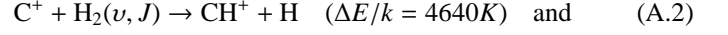
In addition to the chemical state of the gas the TDR model also follows the time-dependent evolution of the level populations of  $\text{H}_2$  in the three different phases, the ambient medium, the active stage, and the relaxation stage. While the code was built to treat up to 318 different levels of molecular hydrogen, we only consider here the first 18 rovibrational levels (with an energy above the ground state smaller than  $10^4$  K) in order to reduce the computation time.

Since the TDR model differs from PDR models by the absence of radiative transfer, neither the UV radiative pumping nor the near- and mid-infrared absorption and induced emission are taken into account. The populations of the excited levels of  $\text{H}_2$  thus results from the combined effects of collisional excitation with H, He, and  $\text{H}_2$  (Flower et al. 1998; Flower & Roueff 1998b,a; Le Bourlot et al. 1999) and spontaneous radiative decay. This latter process is included in the gas cooling function assuming that all the rovibrational lines of  $\text{H}_2$  are optically thin, a hypothesis that holds in the diffuse ISM as long as  $N_{\text{H}} \lesssim 4 \times 10^{24} \text{ cm}^{-2}$  for a gas velocity dispersion of  $1 \text{ km s}^{-1}$ .

### A.4. State-to-state chemical rates

During the past decades, the advances of the cross molecular beam experiments, the flowing afterglow apparatus, the ion trapping techniques, and the theoretical studies of chemical reaction dynamics (see, e.g. the reviews of the field by Casavecchia

2000; Levine 2005) have led to measurements and calculations of state-specific reaction rates for several neutral-neutral and ion-neutral reactions (e.g. Zanchet et al. 2013). In particular the internal energy of  $\text{H}_2$  has been proven to systematically increase the reactivity of highly endothermic reactions (Hierl et al. 1997; Sultanov & Balakrishnan 2005; Zellner & Steinert 1981). To take this process into account, we have implemented in the TDR model a state-specific description of the reaction rates of



For the first reaction, we follow the approach of Agúndez et al. (2010) and adopt the state-specific rate constants of Gerlich et al. (1987) for  $\text{H}_2(\nu = 0, J = 0 \dots 7)$  and the Langevin collision rate for higher energy levels (Hierl et al. 1997). Since there is no information concerning the state-to-state rate constants of reaction A.3, we assume

$$k = \begin{cases} 1.1 \times 10^{-10} \exp\left[-\frac{9860 - E(\nu, J)}{T_{\text{eff}}}\right] \text{ cm}^3 \text{ s}^{-1} & \text{if } E(\nu, J) \leq 9860\text{K} \\ 1.6 \times 10^{-9} \text{ cm}^3 \text{ s}^{-1} & \text{otherwise} \end{cases}, \quad (\text{A.4})$$

where  $E(\nu, J)$  is the energy (expressed in K) of the level  $\nu, J$  of  $\text{H}_2$ .

Comparing the predictions of the model with those obtained without including state-to-state chemistry (Godard et al. 2009), we find that these mechanisms have a little impact on the production of  $\text{CH}^+$  and  $\text{SH}^+$  in the diffuse gas.

### A.5. Electron / ion recombinations on grains and PAHs

Electron transfers between ions and very small grains or polycyclic aromatic hydrocarbons (PAHs) are efficient in decreasing the ionisation state of atoms and molecules (Lepp et al. 1988). When implemented in astrochemical models, such processes are found to compete with (or even dominate) the radiative and dielectronic recombinations of several ions such as  $\text{H}^+$  or  $\text{C}^+$  (Bakes & Tielens 1998; Welty et al. 2003; Wolfire et al. 2008; Hollenbach et al. 2012) and thus to have a strong impact on the hydrogenation chains and the charge balance of carbon- and oxygen-bearing species (see Fig. C.2).

To take these mechanisms into account we have implemented in the TDR code a treatment of the charge of PAHs and very small grains using the formalism described by Bakes & Tielens (1994) and Weingartner & Draine (2001b). Large grains are neglected. Similarly to our treatment of photoreactions, the photoionisation rates of dust particles are modelled using Eq. A.1 with coefficients inferred from the computations of the Meudon PDR code. The electronic attachment and ion recombinations on, respectively, the positively and negatively charged dust particles are modelled using the prescription of Draine & Sutin (1987) and taking into account the electron affinity, the escape length, and the ionisation potentials of the colliders in the computation of the rates (Weingartner & Draine 2001a,b).

Both PAHs and very small grains are described as spherical particles of radius  $6.4 \text{ \AA}$  and  $13 \text{ \AA}$ , respectively. Their abundances in the diffuse ISM are parametrised by the size distribution function of interstellar dust and the dust mass fraction with respect to the gas phase. In this paper we consider a dust-to-gas mass ratio of 0.01 and assume that the PAHs carry 4.6 % of the total dust mass (Draine & Li 2007). The size distribution of PAHs is modelled as a log-normal function centered at  $6.4 \text{ \AA}$  (Compiègne et al. 2011). The size distribution of very

small grains is modelled as a power law with an index of  $-3.5$ . All these considerations lead to  $n(\text{PAHs})/n_{\text{H}} = 4.2 \times 10^{-7}$  and  $n(\text{VSGs})/n_{\text{H}} = 2.5 \times 10^{-8}$ .

## Appendix B: Photodissociation rate of $\text{H}_2$ and $\text{CO}$ : self-shielding

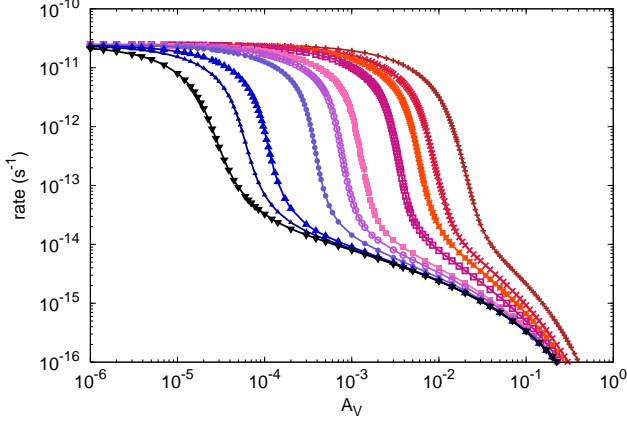


**Figure B.1.**  $\text{H}_2$  photodissociation rate as a function of the extinction computed with the Meudon PDR code applied to PDRs with different densities illuminated on one side: from right to left  $n_{\text{H}} = 10, 30, 50, 100, 300, 500, 1000, 3000, 5000$ , and  $10000 \text{ cm}^{-3}$ , successively.

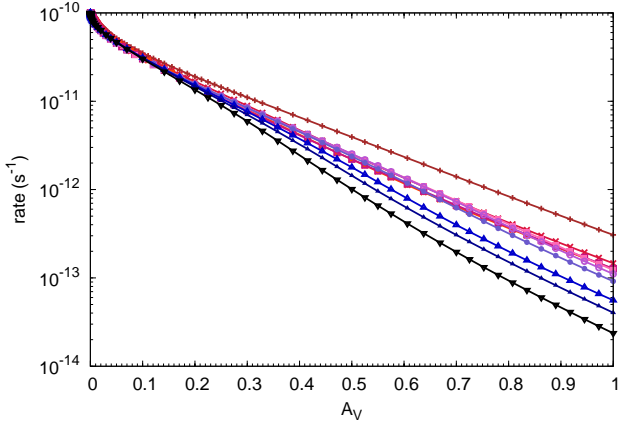


**Figure B.2.**  $\text{CO}$  photodissociation rate as a function of the extinction computed with the Meudon PDR code applied to PDRs with different densities illuminated on one side: from right to left  $n_{\text{H}} = 10, 30, 50, 100, 300, 500, 1000, 3000, 5000$ , and  $10000 \text{ cm}^{-3}$ , successively.

In the standard case of the TDR code, the radiative transfer is modelled with a single parameter  $A_V$ , the extinction of the radiation field in the visible photometric band ( $\lambda \sim 0.551 \mu\text{m}$ ). Such a prescription is, however, too simplistic to correctly describe the photodissociations of  $\text{H}_2$  and  $\text{CO}$  which occur through line processes and therefore strongly depend on the self-shielding

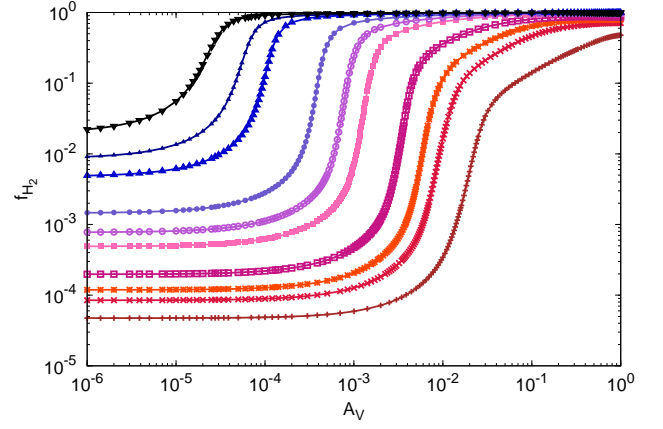


**Figure B.3.** Molecular fraction defined as  $f_{\text{H}_2} = 2n(\text{H}_2)/n_{\text{H}}$  as a function of  $A_V$  computed with the Meudon PDR code for several densities: from right to left  $n_{\text{H}} = 10, 30, 50, 100, 300, 500, 1000, 3000, 5000$ , and  $10000 \text{ cm}^{-3}$ , successively.

(van Dishoeck & Black 1986, 1988). Because these photodissociations drive the chemical transitions from  $\text{H}$  to  $\text{H}_2$  and from  $\text{C}$  to  $\text{CO}$ , it is essential to take into account their dependence on  $A_V$ .

The distinctive dependences of the photodissociation rates of  $\text{H}_2$  and  $\text{CO}$  on  $A_V$ ,  $N(\text{H}_2)$ , and  $N(\text{CO})$  have been studied analytically and numerically by Draine & Bertoldi (1996) and Lee et al. (1996). In their approaches Draine & Bertoldi (1996) consider a directional UV radiation field propagating perpendicularly to an infinite plan-parallel slab of gas, while Lee et al. (1996) apply the approximation proposed by Federman et al. (1979) to solve the self-shielding of  $\text{H}_2$  and  $\text{CO}$ . We have decided to part from these previous studies and to compute the photodissociation rates of  $\text{H}_2$  and  $\text{CO}$  assuming an isotropic radiation field and taking into account the impact of the line broadening on the self-shielding.

The Meudon PDR code was therefore run along a grid of models defined by the following range of parameters :  $10^1 \leq n_{\text{H}} \leq 10^4 \text{ cm}^{-3}$ ,  $0.5 \leq \chi \leq 10$  (in Mathis's units), and  $3 \times 10^{-17} \leq \zeta_{\text{H}_2} \leq 3 \times 10^{-16} \text{ s}^{-1}$ . The code was set to solve the exact transfer within the electronic lines of  $\text{H}_2$  and  $\text{CO}$  assuming a Doppler broadening of  $3.5 \text{ km s}^{-1}$ . While the code is designed to compute self-consistently the formation rate of  $\text{H}_2$  on grain surfaces using both the Eley-Rideal and Langmuir-Hinshelwood mechanisms (Le Bourlot et al. 2012; Bron et al. 2014), we switched off these processes and set the  $\text{H}_2$  formation rate to its observed value of  $3 \times 10^{-17} (T/100\text{K})^{1/2} n_{\text{H}} n(\text{H}) \text{ cm}^{-3} \text{ s}^{-1}$  where  $n(\text{H})$  is the density of atomic hydrogen. The obtained photodissociation rates of  $\text{H}_2$  and  $\text{CO}$  and the predicted molecular fractions of the gas are shown in Figs. B.1, B.2, and B.3 as functions of  $A_V$  and for the subset of models  $\chi = 1$  and  $\zeta_{\text{H}_2} = 3 \times 10^{-16} \text{ s}^{-1}$ .

The obtained photodissociation rates of  $\text{H}_2$  differ from those derived by Draine & Bertoldi (1996) by less than a factor of three for  $N(\text{H}_2) \lesssim 2 \times 10^{21} \text{ cm}^{-2}$  and by more than an order of magnitude for  $N(\text{H}_2) \gtrsim 3 \times 10^{21} \text{ cm}^{-2}$ . The former difference comes from the effect of the line broadening on the self-shielding while the latter is ascribed to the different prescriptions (directional or isotropic) used for the radiative transfer. These interpretations are confirmed with the comparison of our results with those computed by Lee et al. (1996). In this case the photodissociation rates of  $\text{H}_2$  are found to differ by less than a factor of

three over the whole range of  $N(\text{H}_2)$  depending on the values of the density and the cosmic ray ionisation rate  $\zeta_{\text{H}_2}$ .

### Appendix C: PDR and TDR chemical networks

The chemical compositions of photodissociation regions and turbulent dissipation regions are driven by very different chemical patterns. This occurs because the heating of PDRs is dominated by the interaction of UV photons with interstellar matter while that of TDRs is controlled by turbulent dissipation, but also because the state-of-the-art PDR models systematically neglect the gas dynamics and thus solve the at-equilibrium chemical state, while TDR models focus on the non-equilibrium effects, i.e. on the coupling between the dynamics and the chemistry as a function of time. To illustrate these differences we show in Figs. C.1 and C.2 the main production and destruction routes of 27 species including the carbon, sulfur, and oxygen hydrogenation chains as given by the PDR and TDR models. In both cases we show the production pathways obtained locally assuming a diffuse molecular gas of density  $n_{\text{H}} = 50 \text{ cm}^{-3}$ , a shielding  $A_V = 0.4 \text{ mag}$ , and a cosmic ray ionisation rate  $\zeta_{\text{H}_2} = 10^{-16} \text{ s}^{-1}$ . For the TDR model, the results are extracted at the  $r_0$  radius (see Paper I) of an active vortex set by the following parameters:  $u_{\theta, \text{M}} = 3.5 \text{ km s}^{-1}$  and  $a = 10^{-11} \text{ s}^{-1}$ . All these figures are simplified: for each species shown, only the processes that together contribute to more than 70 percent of the total destruction and formation rates are shown.

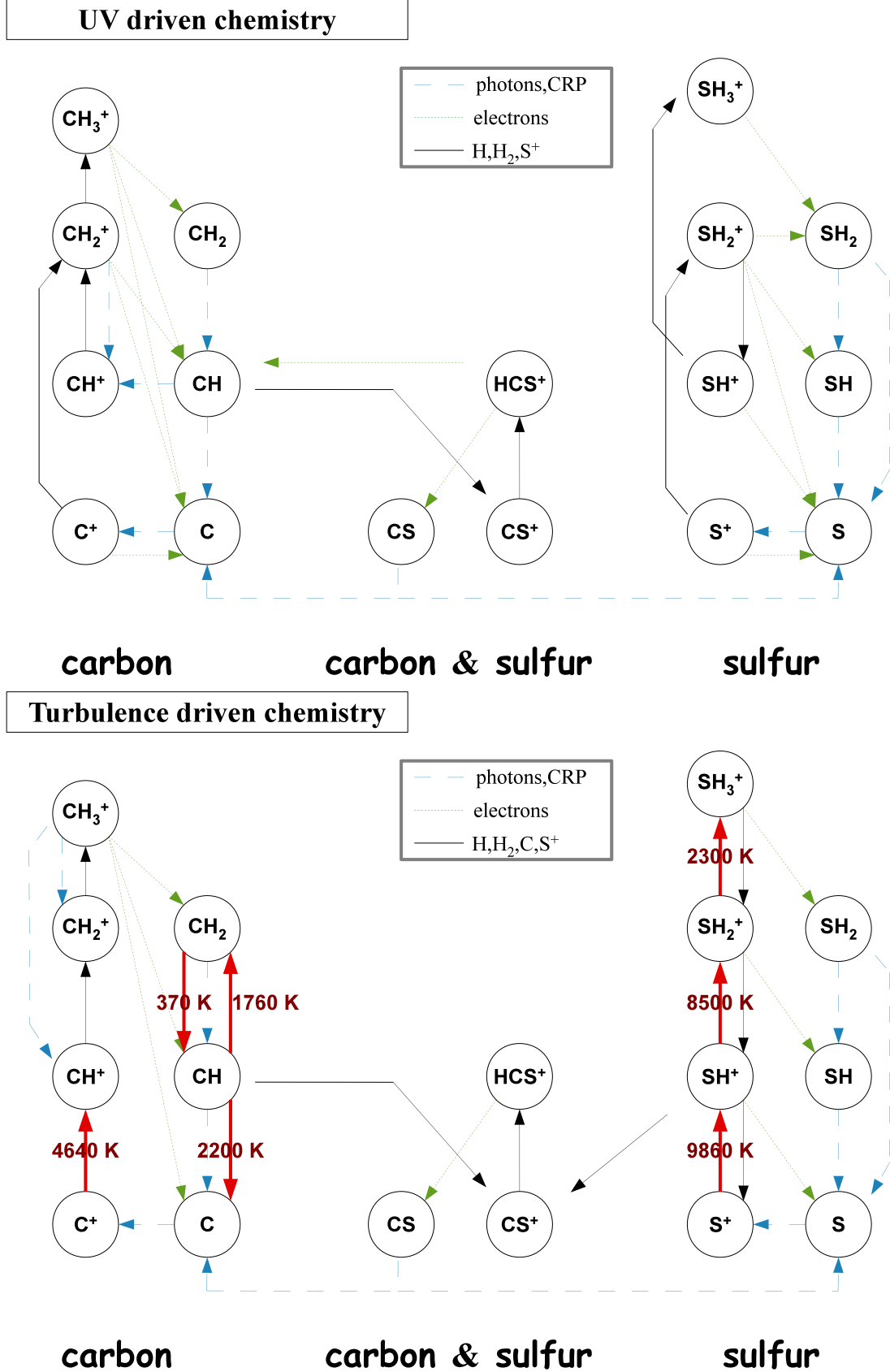


**Figure C.1.** Carbon and sulfur chemical networks driven by the UV radiation field (top panel) and the turbulent dissipation (bottom panel) in the diffuse interstellar medium assuming  $n_{\text{H}} = 50 \text{ cm}^{-3}$  and  $A_V = 0.4 \text{ mag}$ . This figure is simplified: for each species, only the processes that together contribute to more than 70 percent of the total destruction and formation rates are displayed. The endothermicities and energy barriers of endoenergetic reactions are indicated in red.

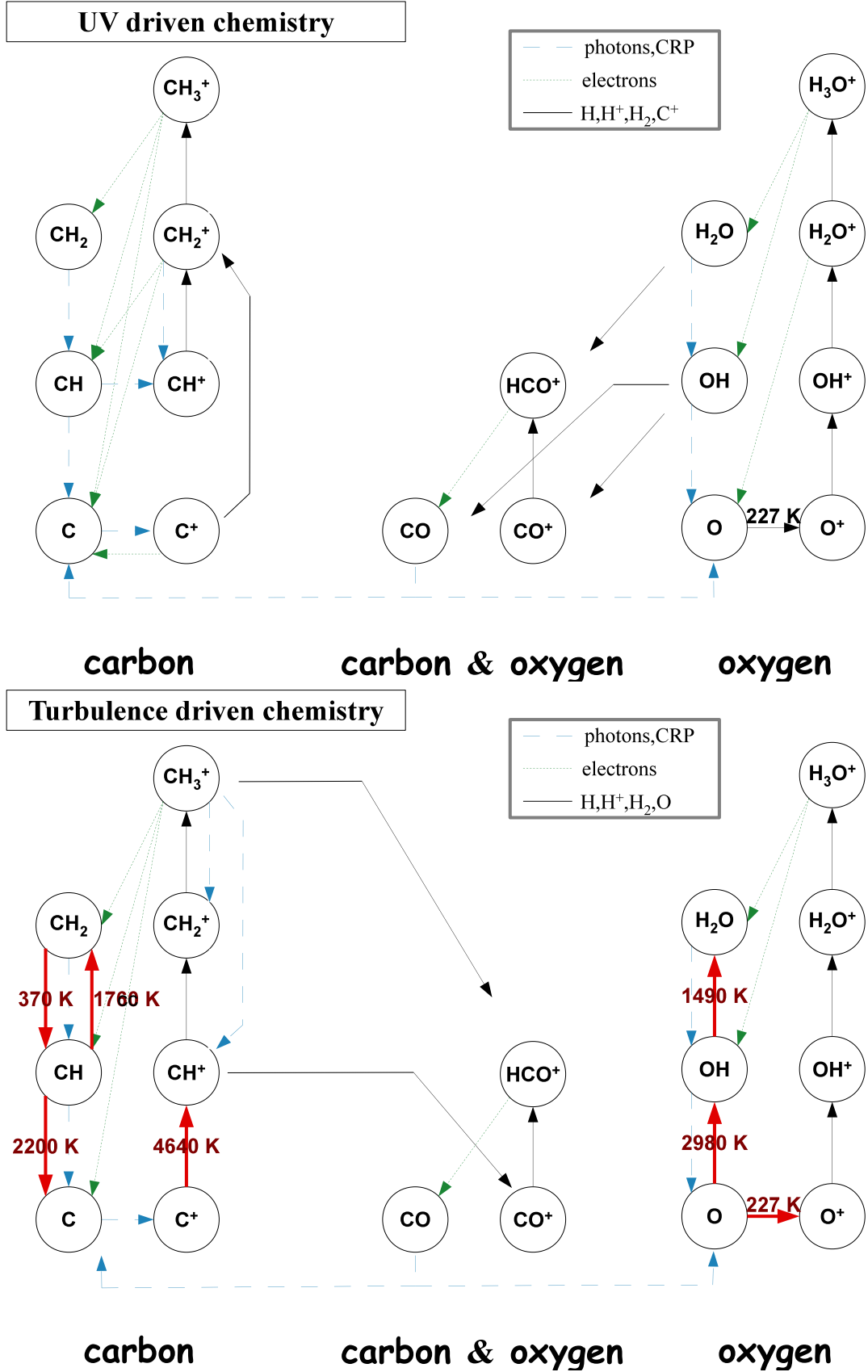


**Figure C.2.** Carbon and oxygen chemical networks driven by the UV radiation field (top panel) and the turbulent dissipation (bottom panel) in the diffuse interstellar medium assuming  $n_{\text{H}} = 50 \text{ cm}^{-3}$  and  $A_V = 0.4 \text{ mag}$ . This figure is simplified: for each species, only the processes that together contribute to more than 70 percent of the total destruction and formation rates are displayed. The endothermicities and energy barriers of endoenergetic reactions are indicated in red.